THESIS

DEVELOPMENT OF A HIGH-EFFICIENCY MICROFLUIDIC DEVICE FOR PRECISE SINGLE CELL ENCAPSULATION

Submitted by

Thomas Leachman

School of Biomedical and Chemical Engineering

In partial fulfillment of the requirements

For the Degree of Master of Science

Colorado State University

Fort Collins, Colorado

Summer 2026

Master's Committee:

Advisor: Sing-Wan Wong

Seth Dillard

Jacob Turner

ABSTRACT

DEVELOPMENT OF A HIGH-EFFICIENCY MICROFLUIDIC DEVICE

FOR PRECISE SINGLE CELL ENCAPSULATION

Microfluidic based single cell encapsulation allows us to control the local microenvironment around individual cells. With a rationally designed microfluidic system, combined with control of flow rates and material selection, we can create homogenous droplets and precisely encapsulate a single cell in one droplet. This approach not only offers highly consistent material properties around individual cells but also protects cells from stress after *in vivo* administration. Single cells encapsulation, hence, can elevate the reliability and predictability of cell-based therapeutic and have been proven effective in directing cellular behavior, such as stem cell differentiation and matrix remodel enzyme production from mesenchymal stromal cells (MSCs). However, most microfluidic systems sacrifice the overall production of droplets to maintain stable flows for droplet homogeneity. This bottleneck significantly reduces the number of functional cells that can be used for therapeutic purposes. This project aims to break the bottleneck and create a highly efficient system that can generate a million single encapsulated cells that meet the needs for therapeutic applications, while maintaining homogeneity, in a much shorter production time. We first designed a multi-parallel flow microfluidic device and utilized ANSYS computational fluid dynamics simulation to predict droplet formation between alginate solution and fluorinated oil as the dispersed phase and continuous phase, respectively. We also simulated the impact of material flow rates, junction dimension, and interfacial tension between alginate and oil on droplet size and formation frequency. After optimizing the parameters, we

fabricated novel microfluidic device for physical experiments for validation. Physical experimentation data suggests that our parallel flow device results in 3.3 times more droplet production, while maintaining droplet homogeneity for over 97%, therefore significantly increasing the yield of homogenous droplet formation when compared to the existing device.

ACKNOWLEDGEMENTS

I would like to thank Dr. Yan Li of Colorado States Design and Merchandising Department for allowing me to use their Theta Flex Tensiometer for enhancing the verification of my project.

TABLE OF CONTENTS

INTRODUCTION

Microfluidic technology in biomedical engineering

Microfluidics refers to the science and technology that manipulates small volume ($x10^{-6}$ liter or below) of fluids in a set system[1]. This technology, to some extent, was inspired by microanalytical methods such as high-pressure liquid chromatography (HPLC) and capillary electrophoresis (CE) in the chemistry field, with these methods leveraging a small volume of a sample to complete the analysis[1]. Around the 1990s, the potential of microfluidic technology has drawn significant attention due to the explosion of genomics science, which requires a substantial amount of molecular analysis with a small sample volume[1]. The need for a high throughput microanalytical tool therefore became one of the fastest-growing fields of technological development. With decades of research advancement, microfluidic technology has now seen revenue in forensic sciences[2], fluid dynamics[3], and has particularly been useful in biomedical fields such as DNA sequencing[4] and drug screening[5,6]. The common advantages of utilizing microfluidics in these applications are high sensitivity, small sample requirements, and low operational costs[7–9].

Microfluidic cell encapsulation: therapeutic potential and current issue

In recent years, cellular investigations using microfluidic systems have emerged as another realm in biomedical applications. Researchers have integrated microfluidic platforms to create small droplets that contain cells, namely cell encapsulation[10,11]. This approach allows researchers to create a specific microenvironment for the cell, hence studying cellular responses. These applications include, long term cell viability[12], proliferation[13], and differentiation[13,14]. Microfluidics has not only been used for studying fundamental biological

questions, one potential application for cellular microfluidic technology is to develop cell-based therapeutics[15]. Cell encapsulation is a desirable therapy due to its ability to conduct sustained release of therapeutic molecules into the body[15]. Encapsulation of donor cells has often been done by utilizing a bulk hydrogels with many cells dispersed inside[16,17]. With this approach, we cannot fully determine the amount of gel volume surrounding individual cell, nor can we predict how cell-cell interactions will contribute to cell fate and functions. Delivery of a bulk encapsulated hydrogel also requires surgery which in turn creates an immune response to repair damaged tissue and to fight infection[18,19]. This leads to the desirability of utilizing single-cell encapsulation, which can create a small product size into micro-meter scale, hence allow direct injection of the engineered cells into the target tissue, avoiding the surgical procedure.

Microfluidic based single cell encapsulation allows us to control the local microenvironment around individual cells. With a rationally designed microfluidic system, combined with vigorous control of flow rates and material selection, we can create homogenous droplets and precisely encapsulate one single cell in one droplet. This approach not only offers highly consistent material properties around individual cells but also protects cells from surrounding challenges after *in vivo* administration. The ability to precisely tune gel volume surrounding individual cells leads to predictable fates and eliminates cell-cell interactions seen inside of a bulk hydrogel which reduces uncertainties of what happens to cells while residing in the hydrogel. Injectable cell therapies can also be achieved with single cell encapsulations to avoid surgery for the patient. Single cell encapsulations therefore can elevate the reliability and predictability of cell-based therapeutics and have been proven effective in directing cellular behavior, such as stem cell differentiation[20] and matrix remodel enzyme production from

mesenchymal stromal cells (MSCs)[21]. However, the majority of microfluidic systems need to sacrifice the overall production of droplets to maintain stable flows that ensure droplet homogeneity. This bottleneck significantly reduces the number of functional engineered cells that can be used for therapeutic purposes. Efforts have been spent on addressing this shortcoming of single cell encapsulation[22–25], but remain to be proven effective to elevate the therapeutic efficiency. This project aims to break the bottleneck, to create a highly efficient system that can generate a million single encapsulated cells that will meet the needs for therapeutic application, while maintaining the required homogeneity, in a much shorter production time.

MATERIALS AND METHODS

Novel multi-parallel device design and Computational Droplet Formation Simulation

The device itself features a flow-focusing junction with microchannels that decrease in width as the fluid spans the device. The previous device designed is shown below in figure 1[20].

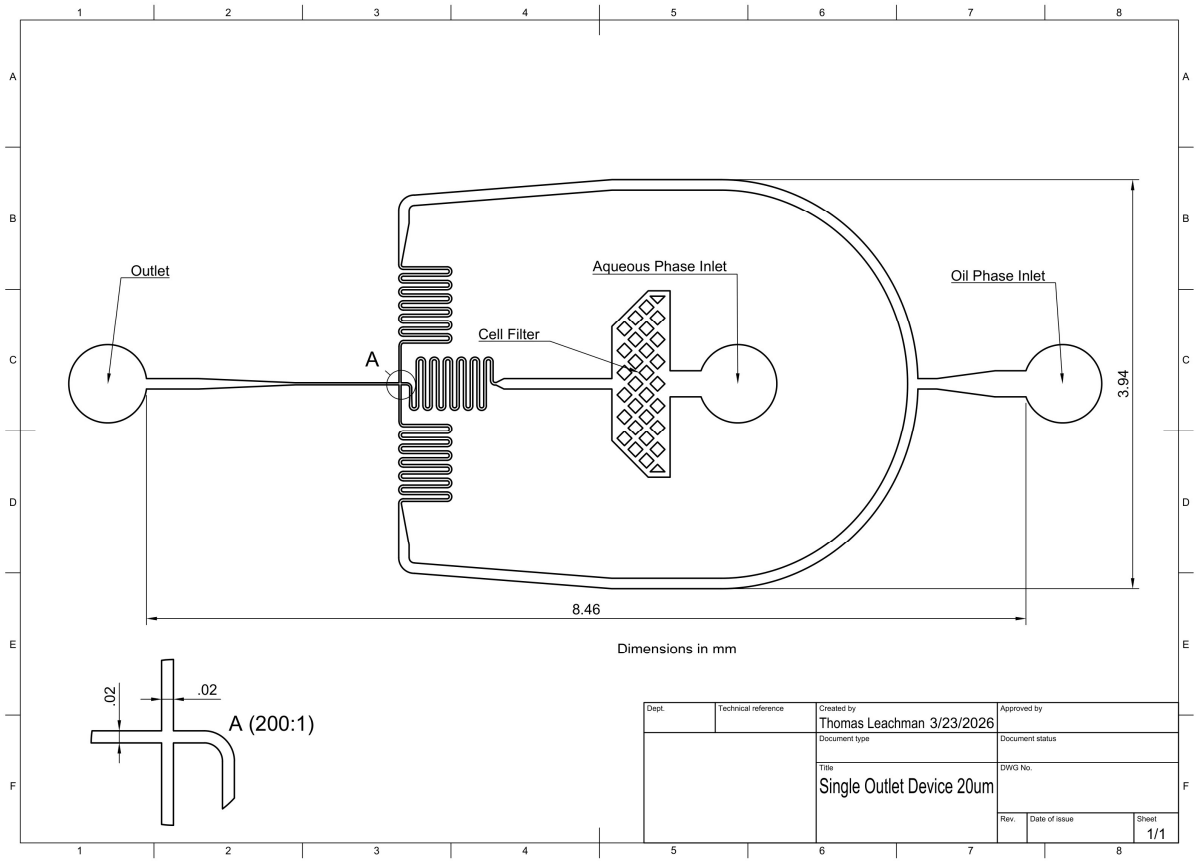

Figure 1: Fusion 360 drawing of single outlet microfluidic flow focusing device

A 2D drawing was made from the existing device seen in figure 1 and populated into Fusion 360. To increase the frequency of droplets while maintaining homogeneity of droplet formation, a new device was designed utilizing similar aspects but with modifications. A parallel flow was inspired from existing literature[29]. Utilizing parallel flow into three junctions stemming from one inlet for the aqueous solution and one inlet for the oil solution allowed us to use a syringe pump

with only two holsters. By increasing flow rates from the two syringes, we would see flow become evenly dispersed amongst the three junctions therefore increasing droplet yield without needing new equipment to power the novel device. The devices were designed to have different junction geometries, one with a 20-micron width, another with a 30-micron width and a third with a 50-micron width. These three devices can be seen below in figures 2-4.

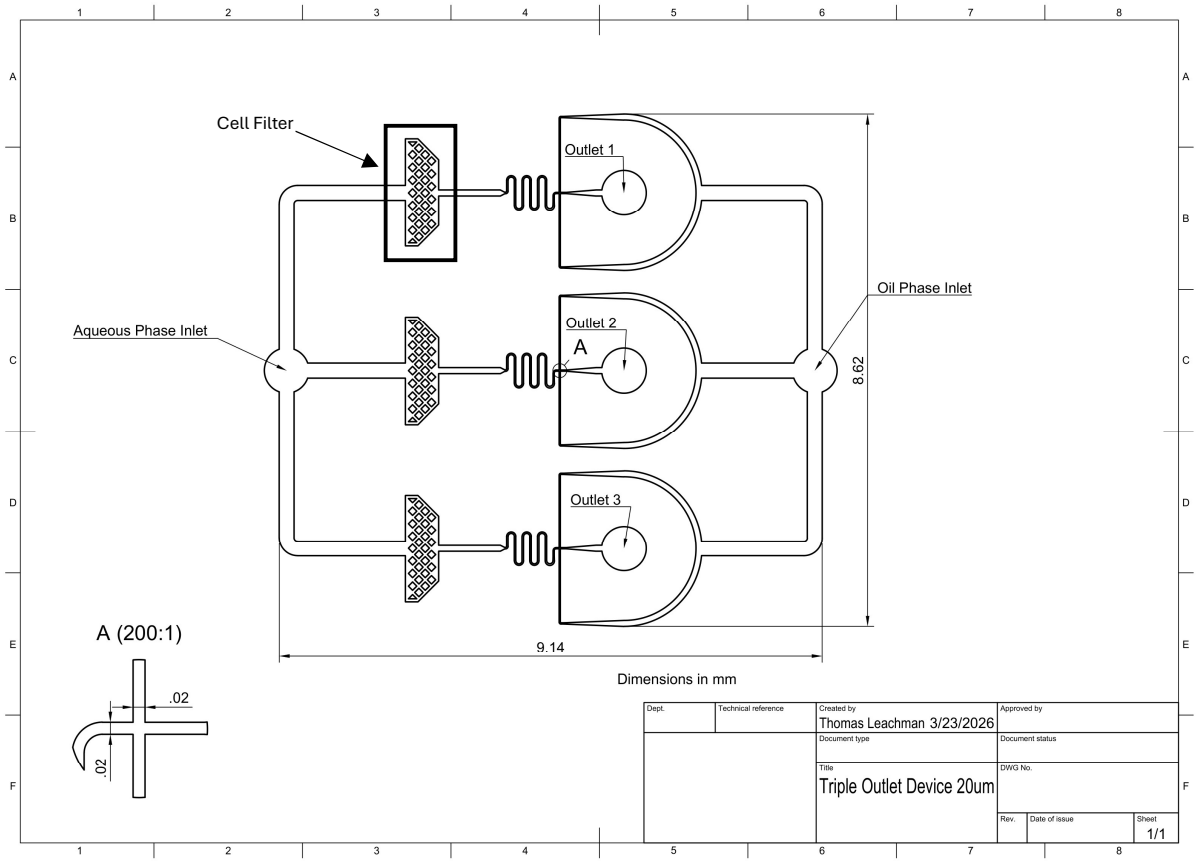

Figure 2: Novel Design 20-Micron Triple Outlet Device

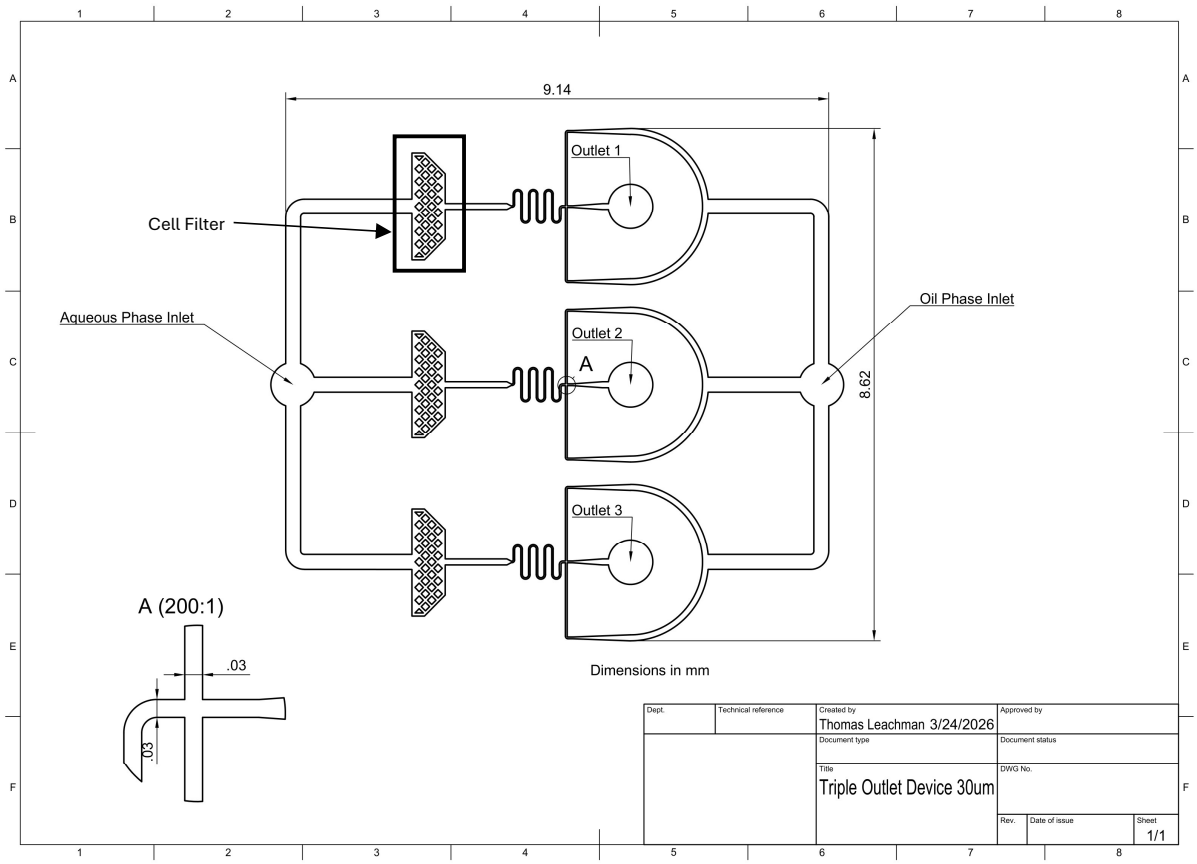

Figure 3: Novel Design 30-Micron Triple Outlet Device

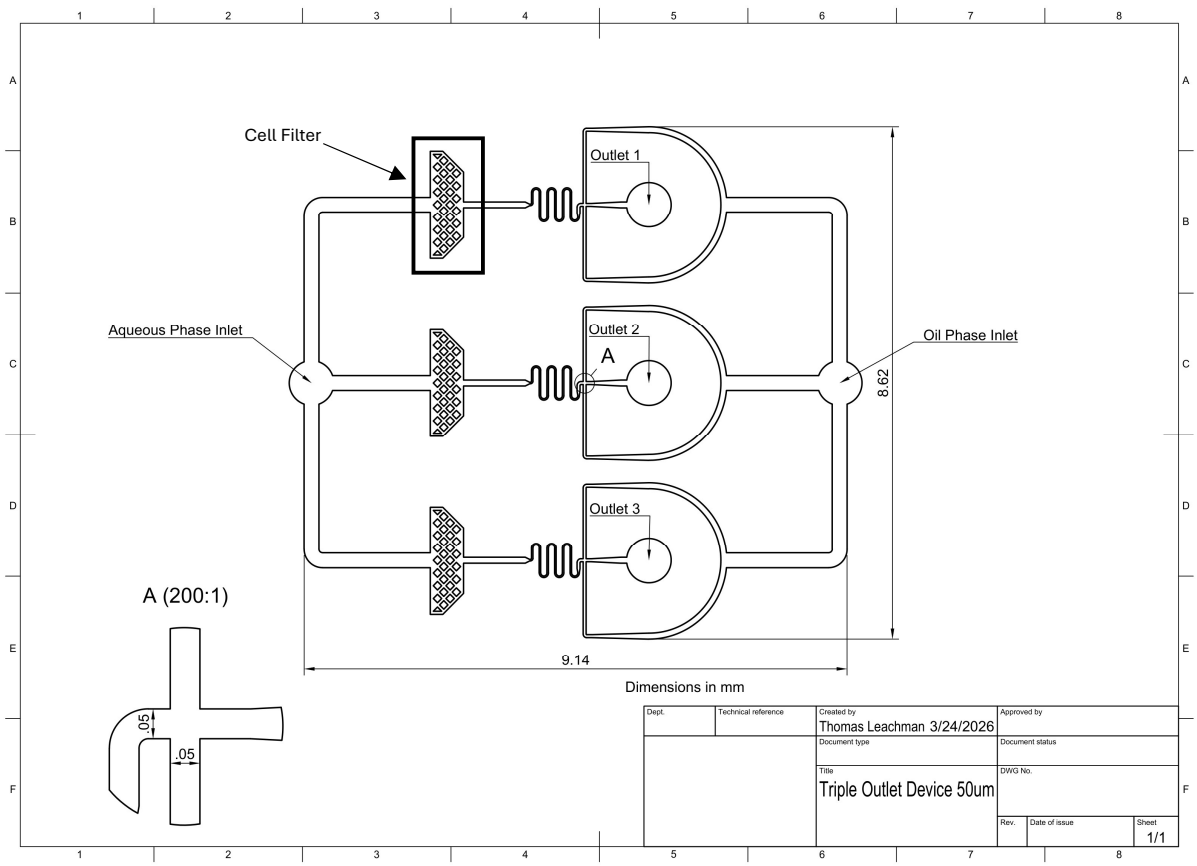

Figure 4: Novel Design 50-Micron Triple Outlet Device

As we can see from figures 2-4, a single inlet is used for both the oil phase and aqueous phase, while the outlet is split into three regions. The aqueous phase inlet and outlet positions have been switched to allow for the single aqueous inlet as it was encapsulated by the oil channels. These three devices still utilize a flow-focusing device layout at the junction with one aqueous inlet and two oil inlets flowing perpendicular to the aqueous phase. Notably we have kept the cell filter, as seen in figure 1, attached to the aqueous phase inlet as well as the splitting, rounded channels that connect to the oil phase inlet. The snaking pattern has also been adjusted to reduce the number of microchannels attached to it for a more efficient manufacturing process. The only area that differs amongst the three devices is the junction width as shown in the bottom left of figures 2-4.

To optimize and understand how droplets will form in the junction of the microfluidic device, computational fluid dynamic simulations via ANSYS Fluent were conducted on the device in various conditions. These conditions included junction size, flow rates of the continuous fluid and dispersed fluid. The continuous fluid is an oil phase, which will not form droplets but will pinch off droplets of the dispersed phase. The dispersed fluid is the aqueous phase, consisting of 1% weight/volume alginate solution in DMEM. The junction itself is what is known as a flow-focusing design, where the dispersed fluid comes from one central inlet and the continuous fluid flows from two perpendicular inlets to meet the dispersed fluid. A flow-focusing device is favored due to its high variety in parameters for controlling droplet size while also producing a high-throughput of droplets due to its symmetric shearing of the dispersed phase[26]. The oil and aqueous phases are immiscible, meaning they will not mix due to their differing intermolecular interactions and molecular structures[27]. This interaction is the beginning of what drives the droplet cutoff paradigm. Droplet formation can be split into three stages: filling, necking and detachment[26]. Filling is the first stage in which the two fluid phases enter the main channel, necking is the reduction of the dispersed phase and detachment is when the dispersed phase droplet breaks off[26]. Viscous forces and interfacial tension between fluids is what drives the necking stage into detachment[26]. A high throughput of droplets forming as well as monodispersity between droplets is of high importance in device design to ensure efficiency and homogeneity. Millions of cell encapsulations are often needed to ensure a successful therapeutic outcome, and it is of upmost importance to ensure each droplet is homogeneous in gel volume. Doing so will enhance the efficacy of a therapeutic response with reliable knowledge on stem cell phenotypes due to its induced surrounding environment. Droplet formation can be categorized into three regimes: squeezing, dripping and jetting[26]. These regimes can be

influenced by the as before mentioned conditions of phase flow rate and junction size. Dimensionless numbers such as the Reynolds number and Capillary can be used to help characterize flow and ensure we create homogeneous droplets in the system. To ensure cells are encapsulated in a homogenous matter, the droplet must be formed within the dripping or squeezing regime. The two variables we can use to better characterize droplet formation include the capillary number denoted as Ca_c and flow rate ratio, denoted as Q, which is the ratio of continuous flow over dispersed flow. It is also noted that the Reyolds number of the system is always within laminar regime due to the slow speed of the fluids and smaller size of the channels. The capillary number shows the relationship of viscous forces over interfacial tension of the fluids. Ca_c is a dimensionless number which helps us with classifying what regime droplets can be classified in and is typically inversely proportional to droplet size. We can see a noticeable shift in droplet formation when $Ca_c=10^{-2}$, this is when droplets tend to transition from forming in the squeezing regime to the dripping regime[28]. Ca_c is written below in equation 1 where U correlates to oil speed, μ correlates to dynamic viscosity and γ correlates to the surface tension coefficient.

$$Ca_c = \frac{U\left(\frac{m}{s}\right) * \mu(Pa.s)}{\gamma\left(\frac{N}{m}\right)} \qquad (1)$$

Dynamic viscosity of the continuous fluid (oil in our case) multiplied by speed of the fluid divided by the interfacial tension of the two reacting fluids is what determines the capillary number. Increasing speed of the oil will increase capillary number, this is the only variable being changed in the microfluidic droplet system. The speed can be a factor of the flow rate as well as the geometry of the microfluidic channels. Increasing the cross-sectional area of the junction will decrease the velocity of fluid if flow rate is kept constant. Shear force is also proportional to fluid

velocity, keeping flow rate constant while increasing cross-sectional area will therefore decrease velocity as well as shear force. With these mechanics in mind, we can tune our device to produce droplets within a selected volume.

With these devices being fully modeled in Fusion 360, we can select a region of interest to utilize in computational fluid modeling (CFD) software such as ANSYS to visualize how droplet formation may occur in a physical test. Utilizing a smaller segment of the entire device reduces the computational expense needed to compute an accurate simulation. For our purposes we highlighted the junction itself as shown in figure 5 below.

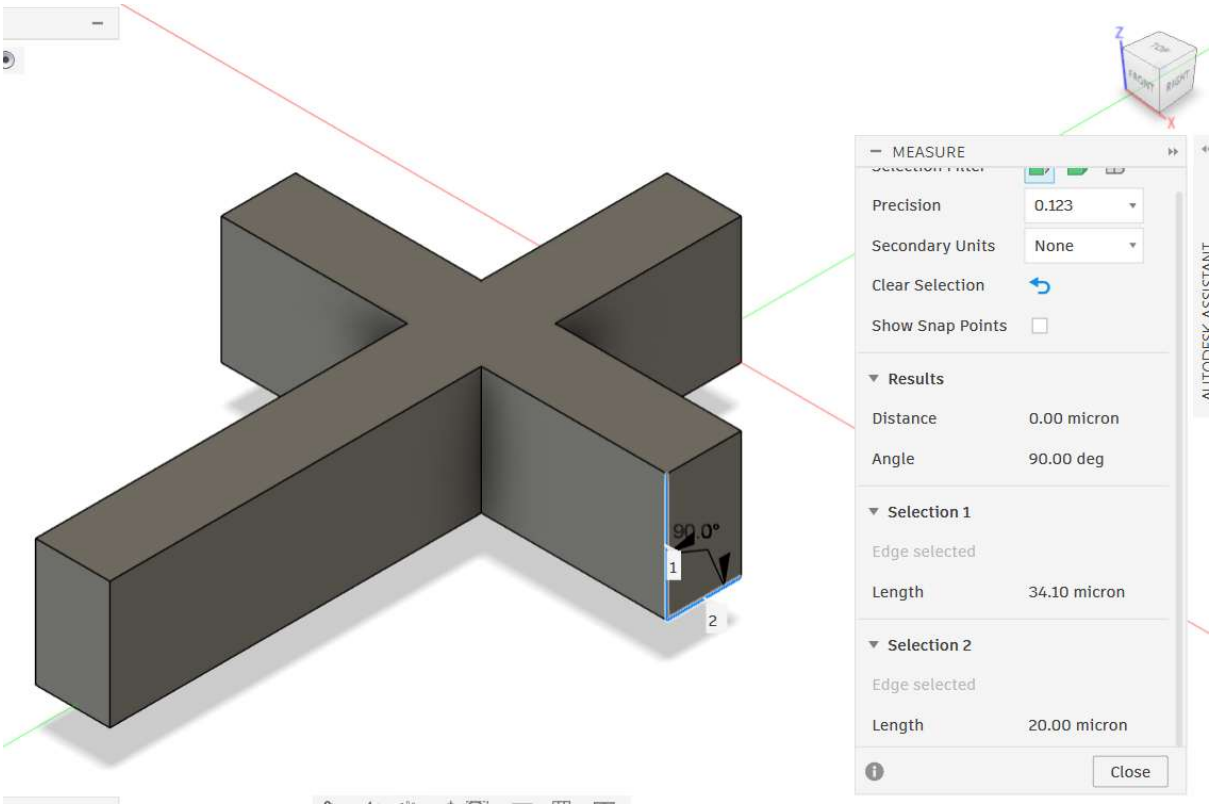

Figure 5: Fusion 360 Snapshot of 20-Micron Junction Used in ANSYS

This region was selected because it is where droplet formation is achieved, making it the most important to validate computationally before moving into physical testing. The most extruded

arm represents the outlet for the junction, the two perpendicular arms from the outlet represent the oil phase inlets and the arm in line with the outlet represents the aqueous phase inlet. This same cutout was utilized from the 30-micron and 50-micron devices as well. The CFD simulation used for these junctions was ANSYS Fluent which soles for the governing Navier-Stokes equations for a multiphase system that utilizes immiscible and incompressible fluids such as the aqueous and oil phases we are evaluating[30].

ANSYS Geometry

The geometries used in the ANSYS software were .step files extracted from Fusion 360. These geometries auto populated into the ANSYS software with the command "import geometry." Figure 6 below shows this imported geometry in DesignModeler.

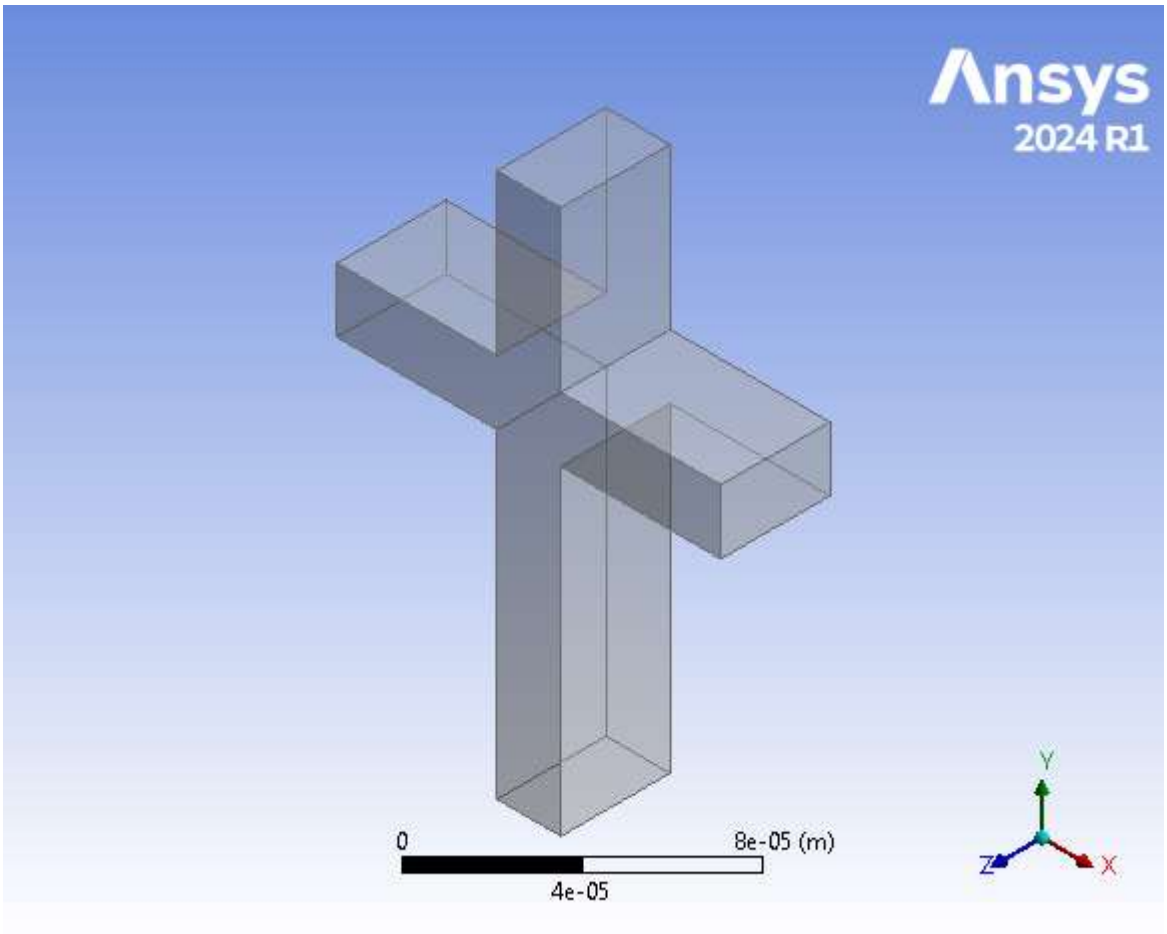

Figure 6: 20-micron Junction Geometry Imported into ANSYS DesignModeler

ANSYS Meshing

The mesh technique for each junction utilizes an automatic method as well as body sizing. The automatic method used the entire geometry as a scope and the method was set to automatic. For body sizing, the entire geometry was selected, and the element size was set to 1.5e-06 m or 1.5 microns. This final mesh is shown below in figure 7. From here the face selection tool was used to create named selections for the geometry with the aqueous inlet, oil inlets, outlet and the rest being walls.

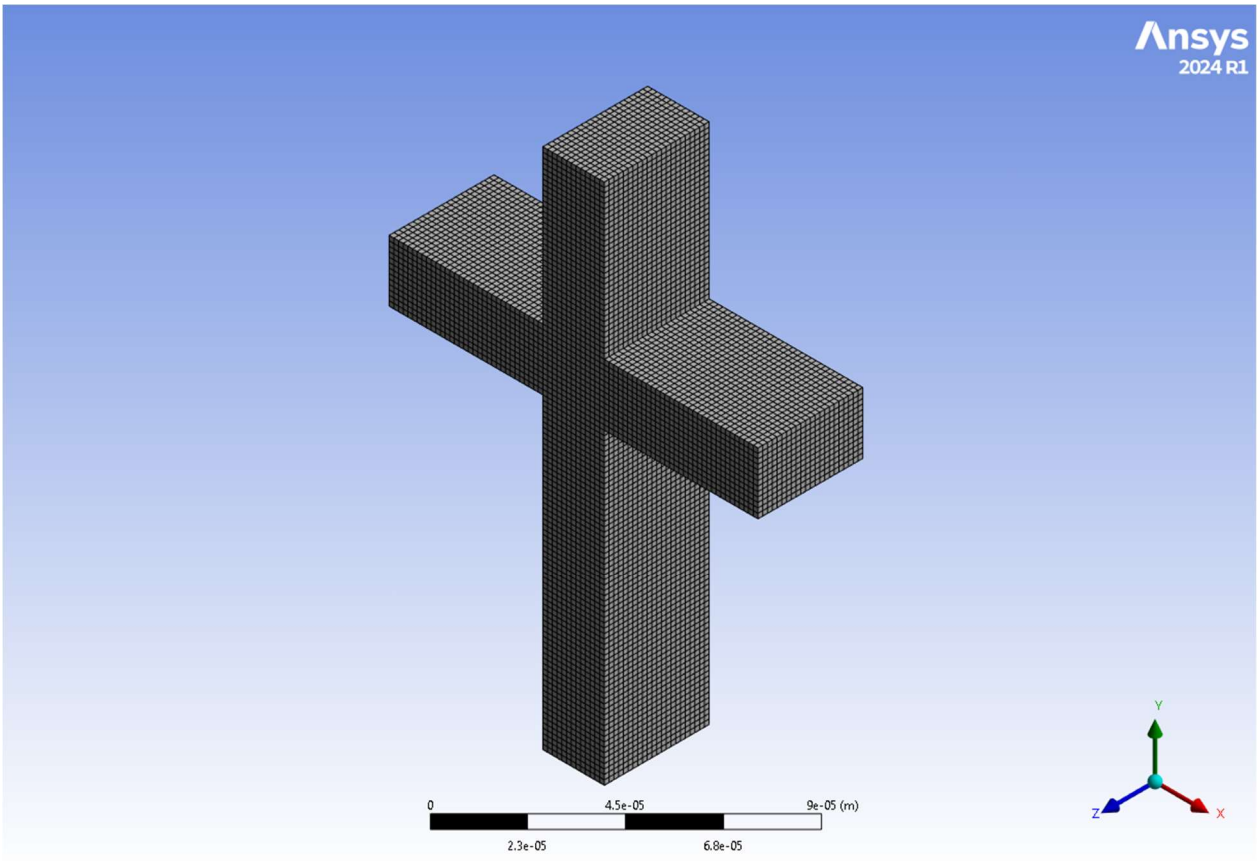

Figure 7: 20-micron Junction Mesh

ANSYS Setup

In ANSYS Fluent Launcher, "double precision" was selected in solver options, and 14 solver processes were used. In general, the solver type was pressure-based, and time was set to transient. In "Models," a multiphase volume of fluid was selected with two eulerian phases, explicit formulation, and sharp interface modeling. Phase 1 or the primary phase was selected to be oil while phase 2 or the secondary phase was the aqueous or alginate phase. The phase interaction was set to have a surface tension coefficient 21.75 N/m which is half of the surface tension coefficient between FO-101 and water. Later this surface tension coefficient was set to be more accurate based on tensiometer testing (tensiometer section in methods). Wall adhesion was also turned on in the global options. The viscous model selection was set to laminar as we know

in this microfluidic device flow will be universally laminar. The two fluid materials created were oil and alginate, respectively. Oil was set to have a constant density of 1550 kg/m^3 and a constant viscosity of 0.00124 kg/(m s)[31]. Alginate was set to have a constant density of 1013 kg/m^3 which was found by weighing known volumes of the fluid and averaging the values. To find the viscosity of the 1% alginate solution a practical test needed to be conducted. The alginate solution is a shear-thinning fluid, meaning as shear increased viscosity decreased, therefore we needed to subject alginate to our practical shear values. The alginate solution was loaded into a hybrid rheometer and underwent a test of increasing shear which is shown in figure 8 below.

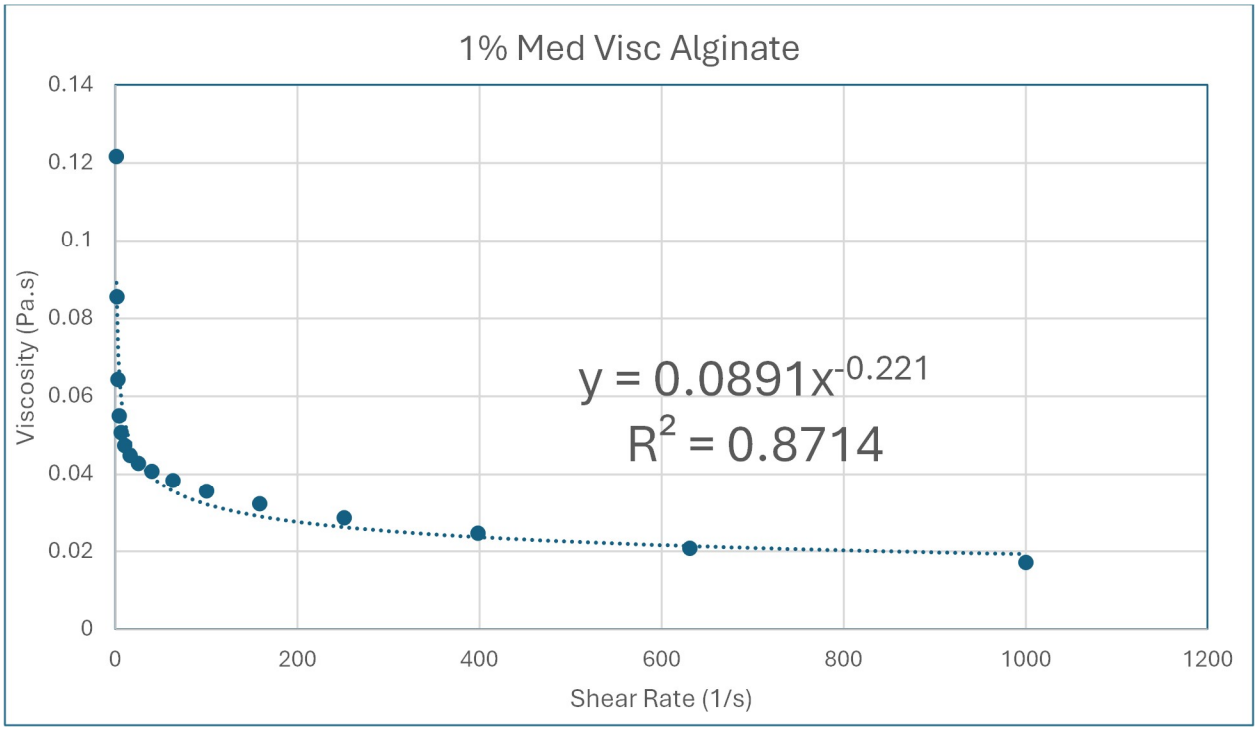

Figure 8: Viscosity vs Shear Rate of 1% Medium Viscosity Alginate in DI Water

Utilizing the equation shown in figure 8 we were able to estimate the viscosity of alginate based on the shear value calculated shown in equation 2 below.

$$Wall\ Shear\ Rate\left(\frac{1}{s}\right) = \left(6 * \frac{speed\left(\frac{m}{s}\right)}{heigh\ (m)}\right) \quad (2)$$

For boundary conditions of the simulation, speed was adjusted for each test to match the flow rates selected. It is worth noting oil phase speed had to be halved as it flows to the junction from two sides, this abides by conservation of mass assuming the oil phase is split evenly amongst the two channels. The wall adhesion selected was a contact angle between phase-1 and phase-2 of 120 degrees to account for the hydrophobic properties of the PDMS walls. Outlet pressure was a gauge pressure of 0 Pa. The solution setup following is elaborated on in more detail in Appendix A. The scheme used was PISO, gradient was Green-Gauss Cell Based, pressure was PRESTO!, momentum was Second Order Upwind, volume fraction was Geo-Reconstruct and transient formulation was First Order Implicit. A hybrid initialization was used with an autosave every 5-time steps. The time advancement of the simulation was fixed with 5000-time steps used at a time step size of $1e^{-6}$ seconds with ten max iterations/time step. The calculation was then run with these parameters' setup. Figure 9 below shows how the geometry import views with blue vectors representing inlets while red vectors show the outlet.

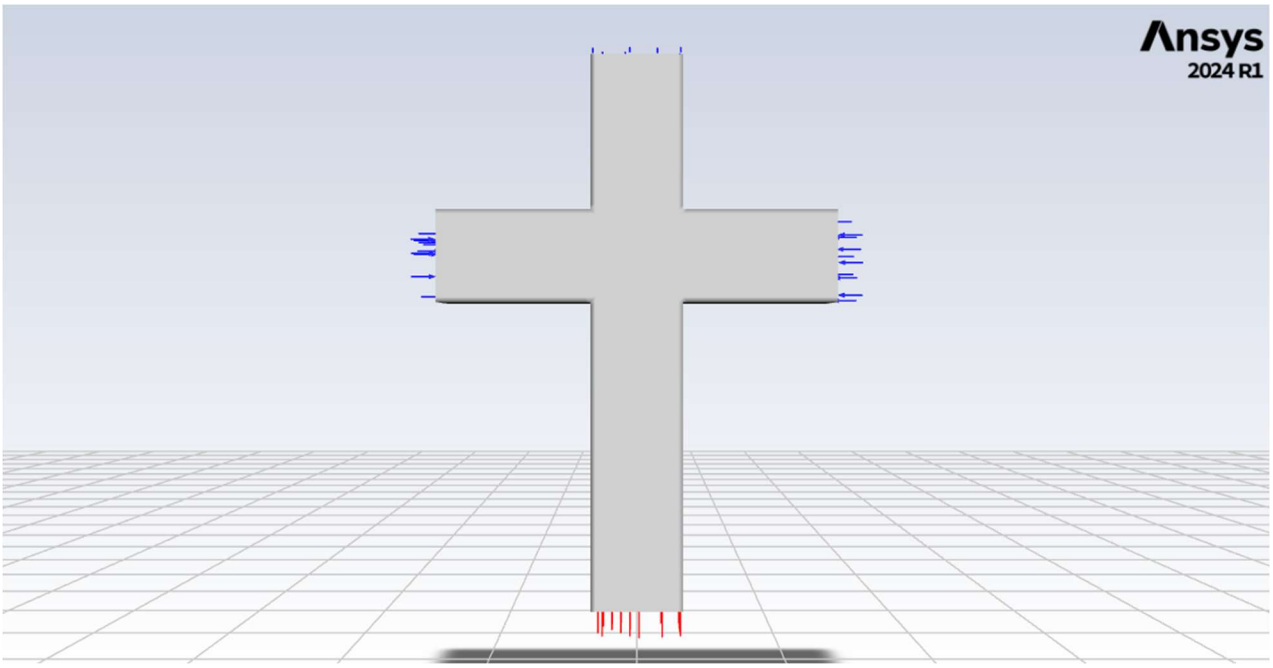

Figure 9: 20-micron Junction with Inlet (blue) and Outlet (red) Vectors in ANSYS Fluent Setup

ANSYS Post-Processing

Once the simulation was completed, CFD-Post was loaded to view the results. A cross-sectional view was created through the center of the XY plane to see the center of the geometry as shown in figure 10.

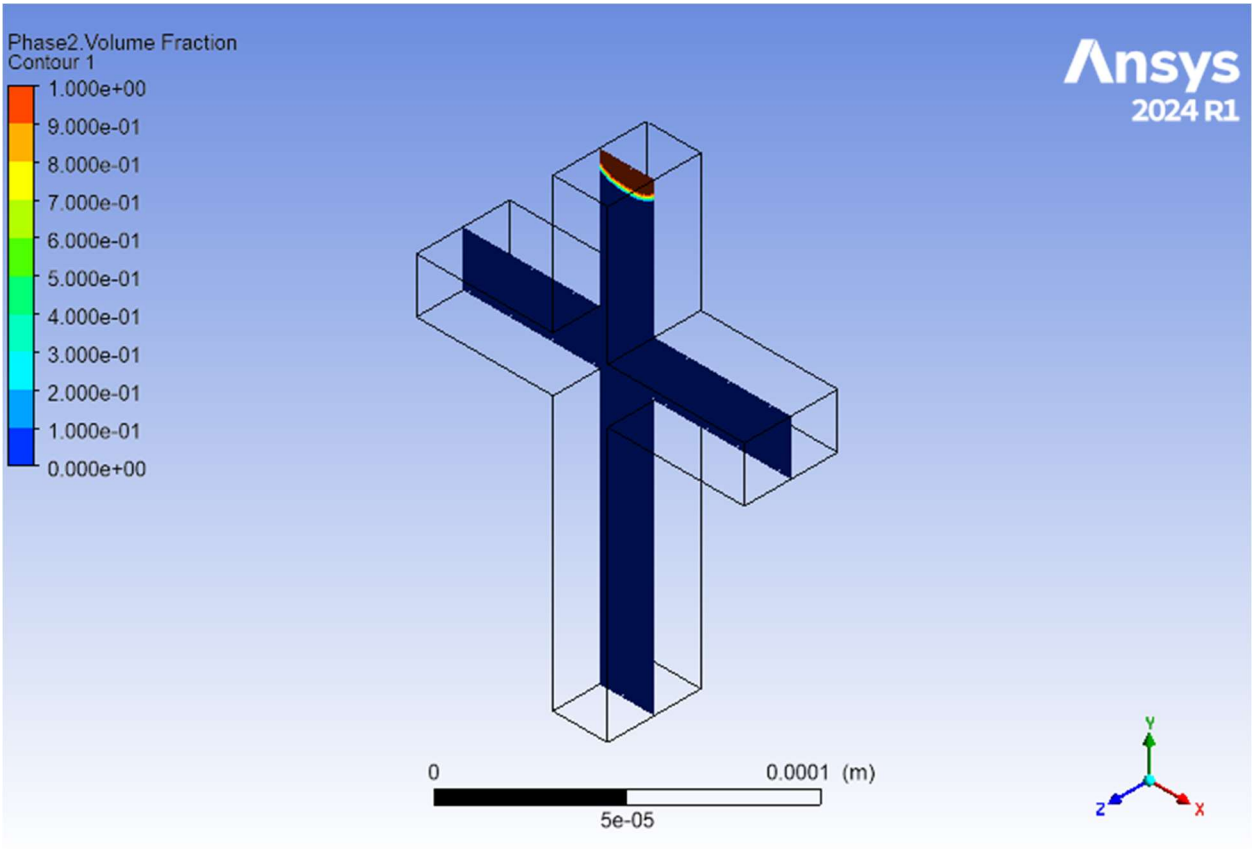

Figure 10: 20-micron Junction ISO View with Mid-Plane Cutout, Oil Phase (blue) and Alginate Phase (red)

This view was most beneficial to see the diameter of each droplet as it moved through the device. While results view as 2D, they are resulting from a 3D simulation. From here, videos were created showing the time-lapse of time steps 5-5000 with each step being 5-time steps as selected in ANSYS Fluent Setup. To further analyze droplet size and frequency of the resulting simulations, ImageJ was used to measure droplet length which subsequently led to calculating droplet volume. Frequency was analyzed by finding the difference in time between two droplets pinching off. By knowing how many time-steps were used in the simulation, we can calculate the actual time each video corresponds to. As stated above, each time step correlates to $1e^{-6}$ seconds. The capillary number for the continuous oil phase is also to be calculated utilizing equation 1. To

compare droplets amongst each other we will look at their volume in micrometers cubed (um^3). We are assuming each droplet is an ellipse as it is bound by the junction geometry, leaving the droplet to only elongate following the plane of direction. The measurements "a" and "b" in equation 3 below are the radius of the droplet along the cross-sectional midplane which would be 10um for both "a" and "b" for the 20µm junction and "c" is half of the length of the droplet.

$$V = abc\pi\frac{4}{3} \quad (3)$$

For the 30µm junction "a" and "b" would be 15um and for the 50µm junction "a" and "b" would be 25um respectively.

Tensiometer Testing

The surface tension coefficient between the FO-101 and alginate has not been reported elsewhere. Therefore, to identify values of the surface tension coefficient between the FO-101 and our 1% medium viscosity alginate solution, a Biolin Scientific Optical Tensiometer or Theta Flex was used. The Theta Flex contains a pendant drop protocol that finds the surface tension coefficient between a droplet and its surrounding media. The Theta Flex utilizes the shape of the hanging drop to interpret the surface tension coefficient due to the balance of forces between two fluids with known density[32]. Since this microfluidic device creates droplets of alginate in a surrounding oil media, we wanted to replicate the same in the Theta Flex procedure. The Theta Flex utilized a syringe holder which can be equipped with a 30-gauge needle. This needle diameter is equivalent to 310 microns. For this setup, alginate would be loaded into the syringe while the syringe needle was engulfed by the FO-101 oil phase which was poured into a clear cuvette. Alginate is less dense than oil so a traditional, vertical hanging droplet technique could not be utilized as the alginate would not hang in the surrounding oil media. Instead, a hooked

needle was used so alginate would be ganging from the needle as its dripping regime would be flowing up the surface of the oil. A diagram of this setup is shown below in figure 11.

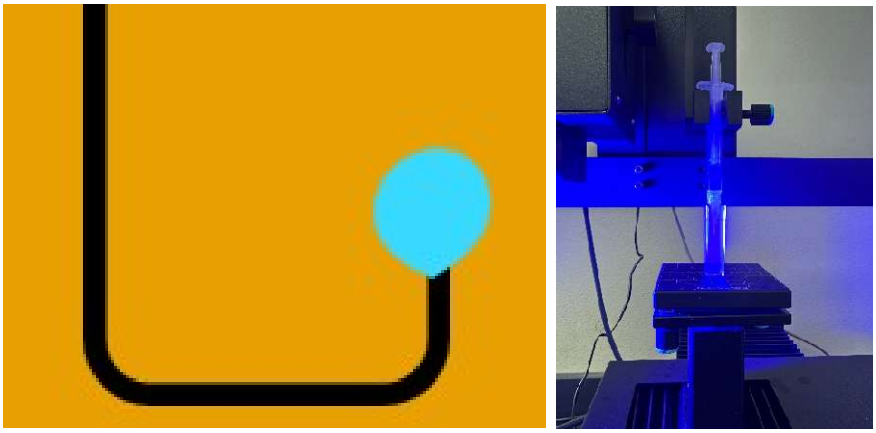

Figure 11: Illustration of Alginate (blue) Pendant Drop Testing in Oil (orange) During Surface Tension Coefficient Measurement and Image from Testing (right)

Physical device fabrication and experimental Setup

Microfluidic Device Fabrication

The chip or master mold for the device was fabricated by FlowJEM. The layout as seen in figure 12 was sent to them to be constructed on a silicon chip.

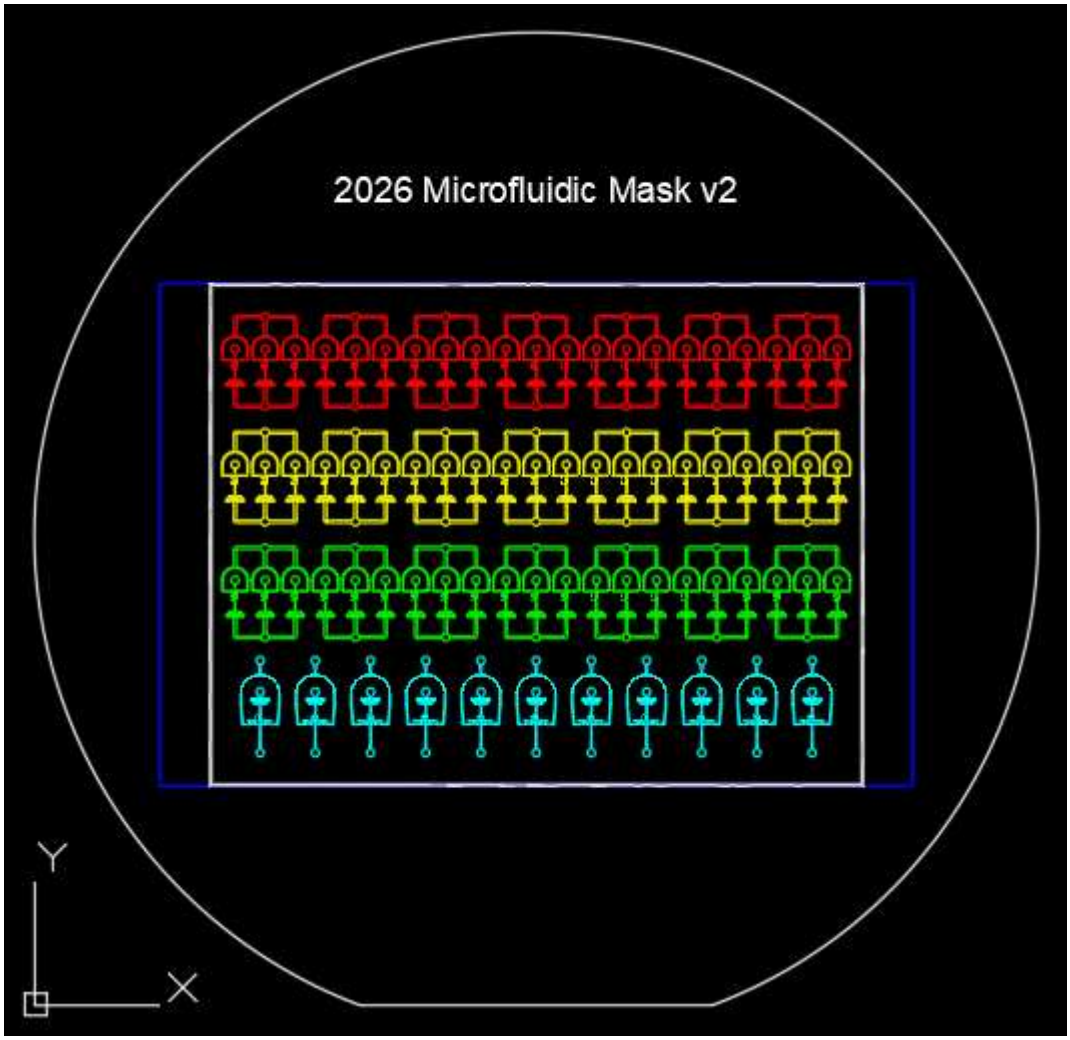

Figure 12: Layout of Microfluidic Devices to be Manufactured on Silicon Chip (20µm Triple in Red, 30µm Triple in Yellow, 50µm Triple in Green, 20µm Single in Blue)

We can see four rows in figure 12, row one corresponds to the 20-micron junction device, row two contains the 30-micron junction device, row three contains the 50-micron junction device and row four contains the original 20-micron junction device that contains one outlet. An SU-8 layer was laid upon the silicon chip with a transparency mask on top of that. The transparency mask contained the layout as seen in figure 12 and a negative photoresist was used to eliminate the covered areas of the transparency mask, leaving the microchannels of the device protruding

upwards of the silicon chip[20]. From this now fabricated master mold we can pour SYLGARD 184 Silicone Elastomer Kit (PDMS) onto the silicon chip to fabricate our devices. The PDMS utilized a 10:1 crosslinking ratio. After mixing the PDMS solution, it was poured on top of the chip and left to degas in a vacuumed chamber for two hours. Once fully degassed the device was placed in a 60 degrees Celsius incubator for 4-6 hours to let the PDMS fully crosslink. Once another PDMS solution was prepared, the crosslinked PDMS could be cut from the device using a standard razor blade which was immediately followed by a new layer of PDMS to preserve the device's integrity. The process was once again repeated and stored in the crosslinked PDMS until another device needed to be fabricated. Once the crosslinked PDMS device was cut from the master mold, each inlet and outlet needed to be punched out using a WellTech Rapid-Core 1mm biopsy punch. To prepare the PDMS for plasma bonding, 3mm scotch tape was used to remove dust and other small particles that may have attached themselves to the PDMS. The same was done for a glass slide. Utilizing the MTP3 plasma bonder, plasma was introduced to the PDMS device on the microchannel side, this same technique was used on the glass slide to ionize both surfaces to prepare them for adhesion. The plasma bonder was swept onto both surfaces in 10 second intervals for a total of one minute. The PDMS device was immediately pressed onto the adjacent glass slide; the now adhered device underwent incubation at 60 degrees Celsius for 4-6 hours to fully bond the two surfaces.

Oil Phase Solution

The oil phase solution was composed of three ingredients: FO-101, 157 FSH Oil (surfactant) and acetic acid. Two different oil phase mixtures were used, one containing 1% surfactant and another with 2% surfactant. The solvent of the oil phase consisted of FO-101 (98-

99%). Acetic acid made up 0.01% of the solution in both mixtures. This was often made in 1mL or 1.5mL aliquots.

Alginate Phase Solution

Alginate is a natural polymer extracted from brown seaweed, it is a hydrophilic and water-soluble material and forms a hydrogel when divalent cations are presented in the solution[33]. Alginate can be used in differing viscosities and molecular weights, higher concentrations of polyvalent cations also effect the amount of cross-linking that occurs between alginate chains[33]. The divalent cation used in hydrogel synthesis is calcium carbonate. Manipulating these cofactors of alginate allows us to finely tune the mechanical properties of our hydrogels to ensure encapsulated cells reside in an environment that mimics organic tissue. The alginate or aqueous phase solution was made with a lyophilized medium viscosity alginate. The lyophilized alginate was made into a 1% weight/volume solution with FluoroBrite DMEM as the solvent. This solution was then mixed using an orbital shaker until the alginate was fully dissolved. Once mixed, 999 microliters were extracted into a separate tube. In this tube, one microliter of a 10% weight/volume solution made of calcium carbonate in DMEM was added. This created a 0.01% calcium carbonate solution in a 1% medium viscosity solution in DMEM.

Droplet Production

Physical testing of the devices was conducted utilizing a Harvard Apparatus Pump 33 DDS (Dual Drive System) Syringe Pump, the PDMS-glass slide bonded microfluidic devices, a plastic 3mL BD syringe, a plastic 1mL BD syringe, the oil and aqueous phase solutions and 1mm diameter tuning. Once the oil phase was loaded into a 3mL syringe and the alginate phase loaded into a 1mL syringe, 27-gauge BD PrecisonGlide needles were attached to the lure locks on the syringes. Medical tubing denoted as 95 Durometer LDPE (0.015” inner diameter, 0.043” outer

diameter) was cut and fitted over each needle. The syringes were loaded into the syringe pump and locked into place. The medical tubing was fitted into each respective inlet utilizing tweezers, the outlets were also fitted with their own medical tubing that led into a single collection tube as shown in figure 13 below.

Figure 13: Device Fully Fitted with Medical Tubing with Close-up View

Once the device has been fully fitted as seen in figure 13, flow rates were selected for each syringe in microliters per minute (µL/min) such as 3µL/min for the oil and 1µL/min for the alginate. The device was left to run for a designated amount of time that depended on the experiment, which was typically 15-30 minutes, the criteria to stop droplet production was if the run failed or the collection tube was filled to approximately 200 microliters. Droplets were collected in the tube and imaged utilizing a swift imaging camera fitted to a microscope.

Droplet Analysis

From droplet images we can find an average diameter amongst the population. For our purposes, we randomly selected 30 droplets from each image and analyzed the diameter of each

one. Averaging these 30 values will give us an average droplet diameter in the sample. To quantify the homogeneity of the droplets, a coefficient of variation was calculated to give us a percent value that relates to the variation between diameter measurements. Equation 4 shows this relationship where a smaller percentage relates to less variation.

$$COV(\%) = \frac{standard\ deviation}{mean\ diameter} * 100 \quad (4)$$

Equation 5 below shows how to calculate frequency of droplets based on droplet volume (V_d) and the aqueous or alginate phase flow rate (Q_d).

$$Frequency\left(\frac{droplets}{second}\right) = \frac{Q_d\left(\frac{uL}{s}\right)}{V_d(uL)} \qquad (5)$$

RESULTS

ANSYS Simulations on Droplet Formation

ANSYS simulations were saved as video files which were then used for further evaluation based on droplet size and frequency of droplet production. The representative video snapshots used for evaluation are shown in figures 14-16 below.

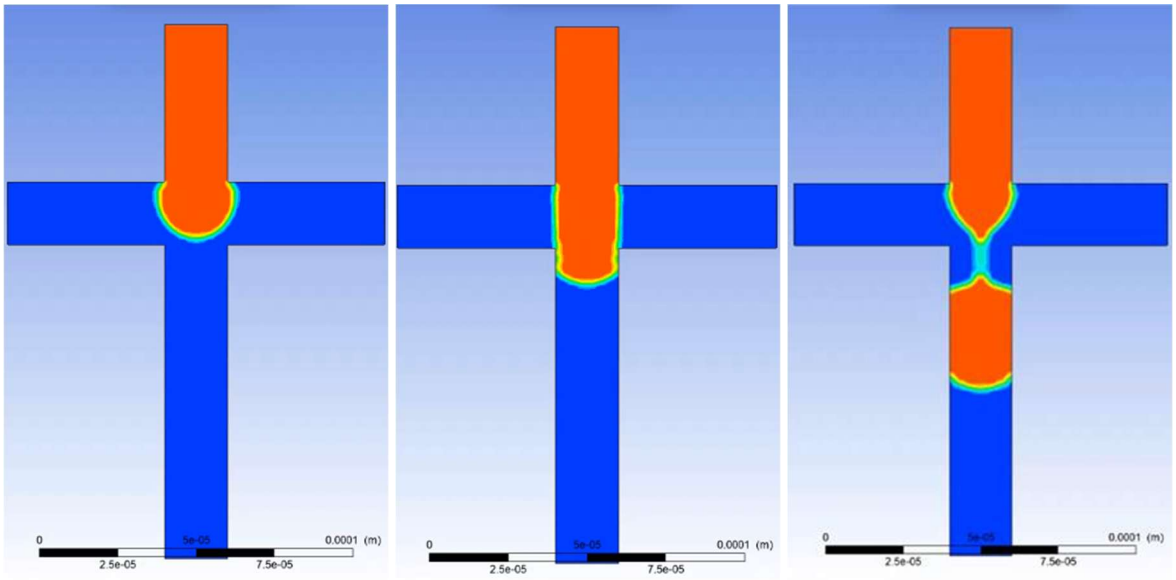

Figure 14: 20-Micron Junction with Flow Rates of Oil=3µL/min and Alginate=1µL/min (time steps of 2.68ms, 3.05ms and 3.41ms)

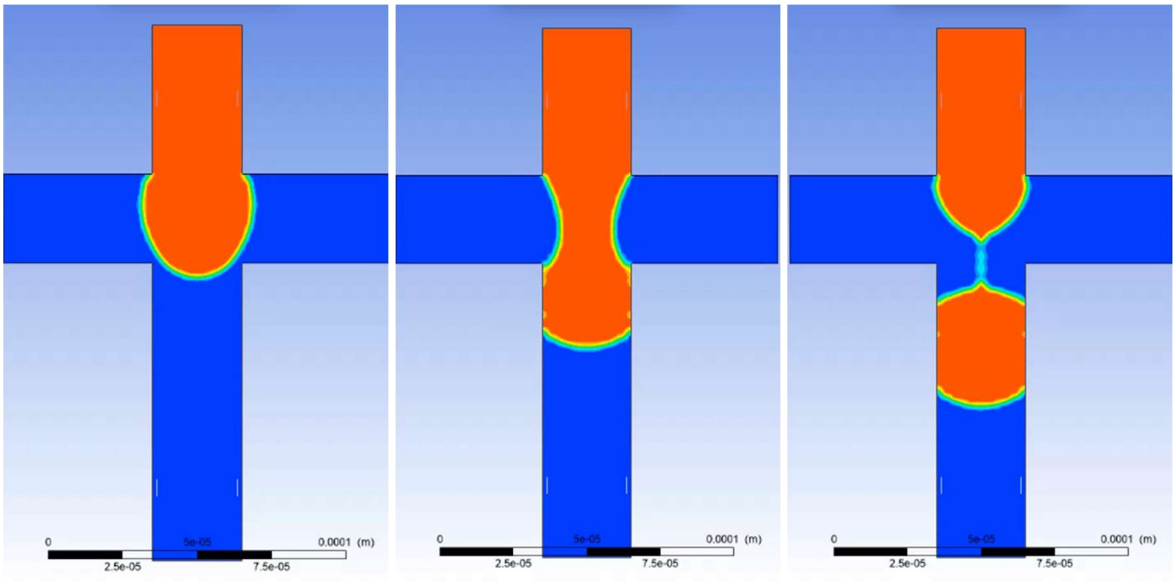

Figure 15: 30-Micron Junction with Flow Rates of Oil=3µL/min and Alginate=1µL/min (time steps of 4.94ms, 5.42ms and 5.78ms)

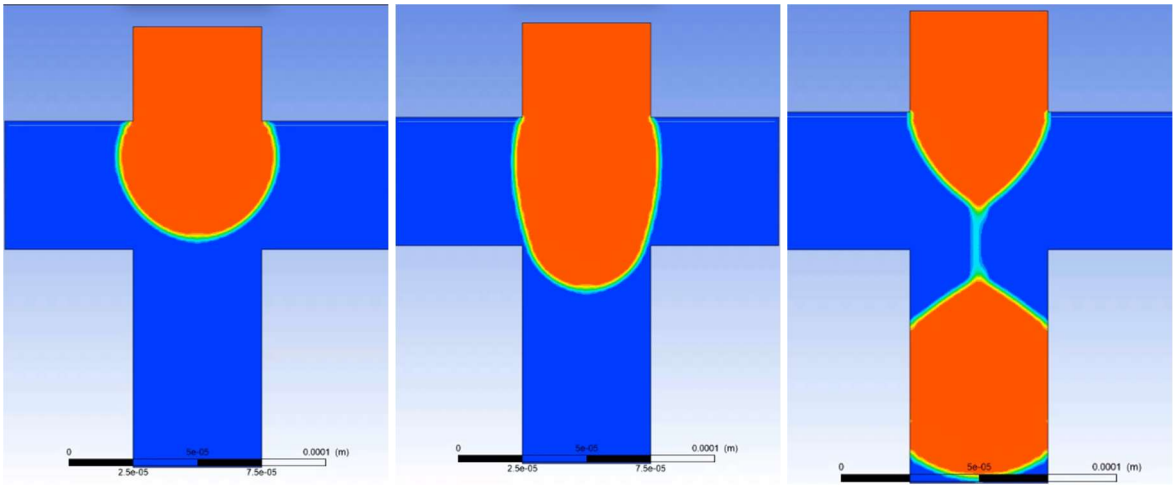

Figure 16: 50-Micron Junction with Flow Rates of Oil=3µL/min and Alginate=1µL/min (time steps of 8.1ms, 9.92ms and 11.73ms)

Figures 14-16 show the same flow rate ratio of 3 to 1 between oil to aqueous at the three junctions and the time steps taken for the first droplet to form. This ratio was chosen as a baseline between the three to see how droplets change based solely on geometry of the device.

Figures 17-20 below demonstrate how changing the flow rate within the 20-micron and 30-micron junctions changes droplet production.

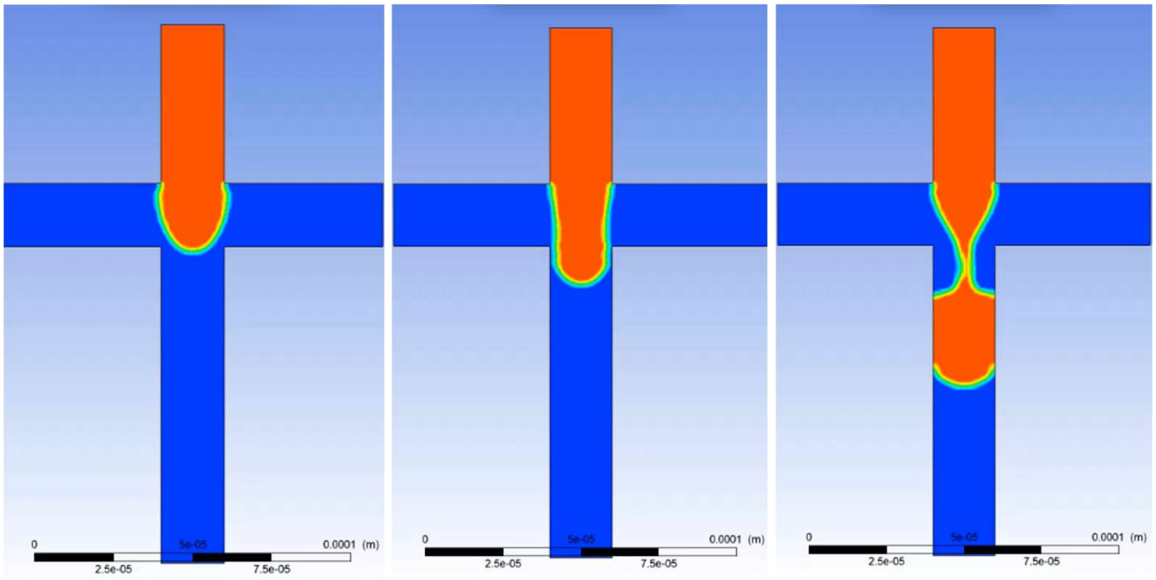

Figure 17: 20-Micron Junction with Flow Rates of Oil=10µL/min and Alginate=1µL/min (time steps of 2.64ms, 2.76ms and 3ms)

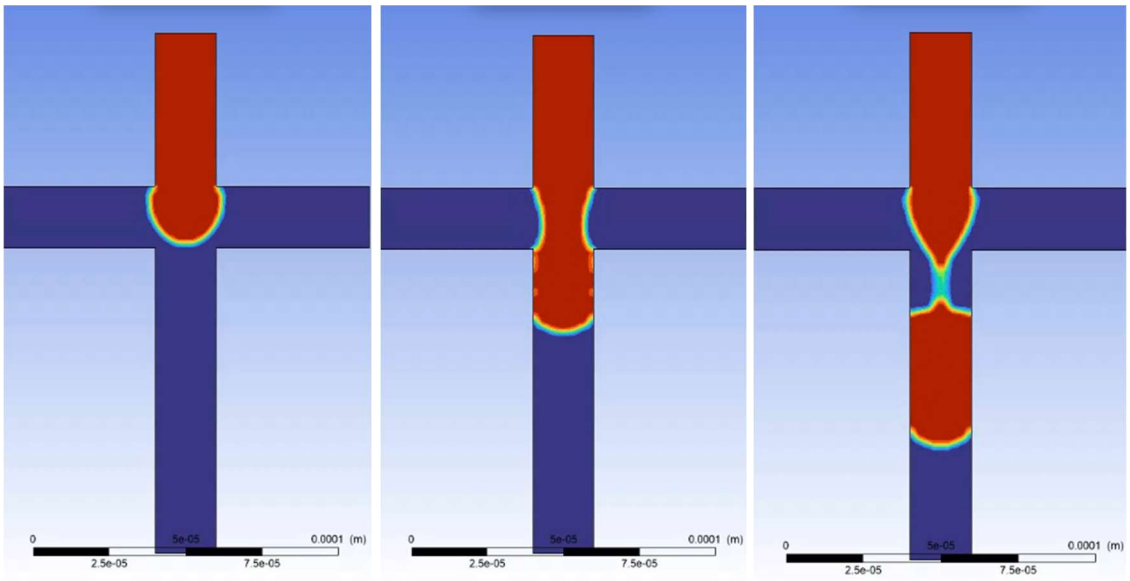

Figure 18: 20-Micron Junction with Flow Rates of Oil=6µL/min and Alginate=2µL/min (time steps of 1.32ms, 1.56ms and 1.8ms)

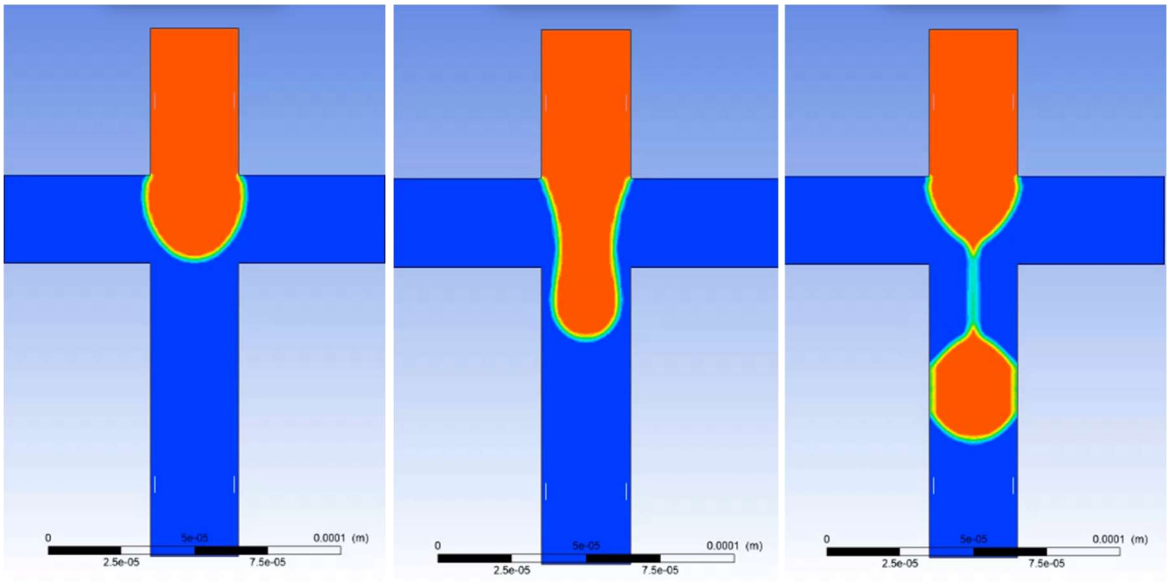

Figure 19: 30-Micron Junction with Flow Rates of Oil=10µL/min and Alginate=1µL/min (time steps of 4.46ms, 4.82ms and 5.18ms)

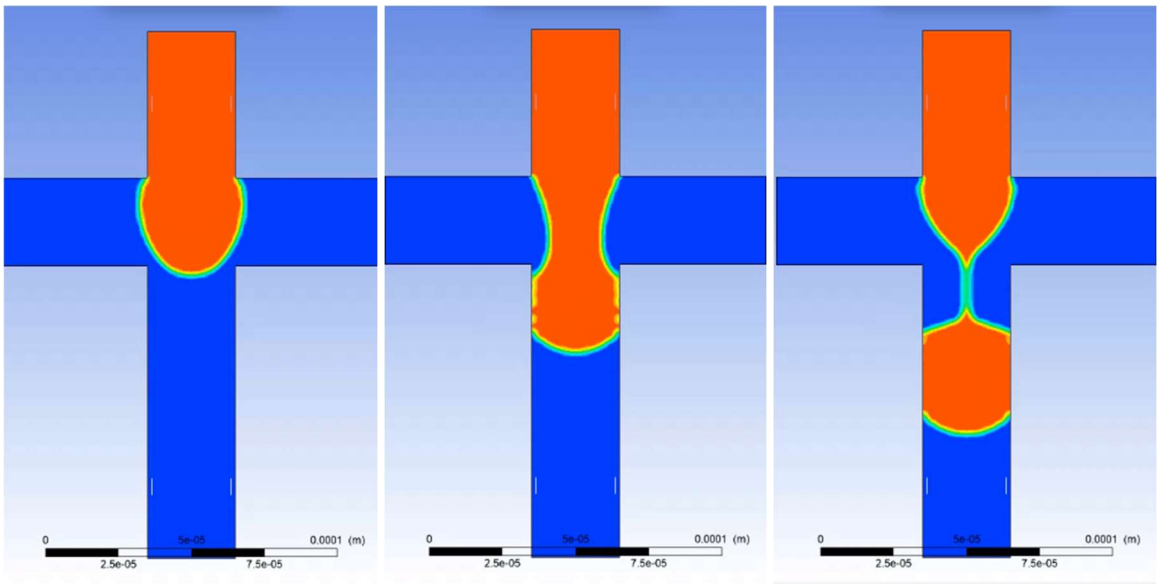

Figure 20: 30-Micron Junction with Flow Rates of Oil=6µL/min and Alginate=2µL/min (time steps of 2.4ms, 2.64ms and 2.88ms)

From these simulations we can find droplet length using ImageJ, droplet length was selected as droplets show to be pushed against the walls meaning the droplet width while it remains in the

channel correlates to channel width. The capillary number (Ca_c) was also found for these simulations.

Table 1: Droplet Volume, Frequency in Droplets per Second and Capillary Number for Each Simulation

Simulation	Droplet Volume (um^3)	Frequency (droplets/second)	Ca_c
20µm Q=3/1	5,542	996	0.0042
30µm Q=3/1	16,621	520	0.0028
50µm Q=3/1	85,556	160	0.0017
20µm Q=10/1	5,226	1700	0.0139
30µm Q=10/1	10,824	806	0.0093
20µm Q=6/2	6,356	1960	0.0084
30µm Q=6/2	14,665	1092	0.0056

From the ANSYS results we can analyze how droplet behaviors depend upon flow rate and geometry. First, we can analyze the 20µm junction results from table 1. For a flow rate ratio (Q) of 3/1 (oil flow rate over alginate flow rate) we see droplet volume equal to 5,542um^3 with a frequency of 996 droplets per second and a capillary number of 0.0042. When compared to the same junction size with Q=10/1, droplet volume decreases to 5,226um^3 while frequency and capillary number increase to 1700 droplets per second and 0.0139 respectively. When the same 20µm junction is subject to Q=6/2, we increase both flow rates proportionally to maintain the same ratio of Q=3. From this simulation we see a droplet volume of 6,356um^3, frequency of

1960 droplets per second and capillary number of 0.0084. These droplets remained in the dripping regime, but droplet volume increased by 1.15 times that of the original Q=3/1 test. By keeping Q=3 we would expect to see droplets that are of similar size, yet our results did not abide by this rule. For our 30µm device the same three Q's were simulated: 3/1, 10/1 and 6/2. For Q=3/1, droplet volume increased to 16,621um^3, frequency dropped to 520 droplets per second, and the capillary number dropped to 0.0028. When we increase Q=10/1 in the same 30µm junction, droplet volume decreases to 10,824um^3, frequency increases to 806 droplets per second and the capillary number also increases to 0.0093. The same trend of decreasing droplet length while increasing frequency is seen here as it is with the 20µm junction. However, the droplet length decreases dramatically with this increase in cross-sectional area leading us to believe that junction geometry has large effects on droplet behavior. The 30µm Q=6/2 simulation gives us a droplet volume of 14,665um^3, a frequency of 1092 droplets per second and a capillary number of 0.0056. In comparison with the 30µm Q=3/1 simulation, when increasing both flow rates while keeping Q=3, the 30µm junction gives smaller droplets while the 20µm junction in this same comparison gave larger droplets. 50µm junction test at Q=3/1 where droplet volume is increased to 85,556um^3, frequency is decreased to 160 droplets/second, and the capillary number is decreased to 0.0017.

Tensiometer Analysis on Interfacial Tension Between Oil and Alginate

The Theta Flex was utilized to find a more accurate surface tension coefficient between the oil and alginate solutions. Figure 21 below shows a snapshot of the imaging setup.

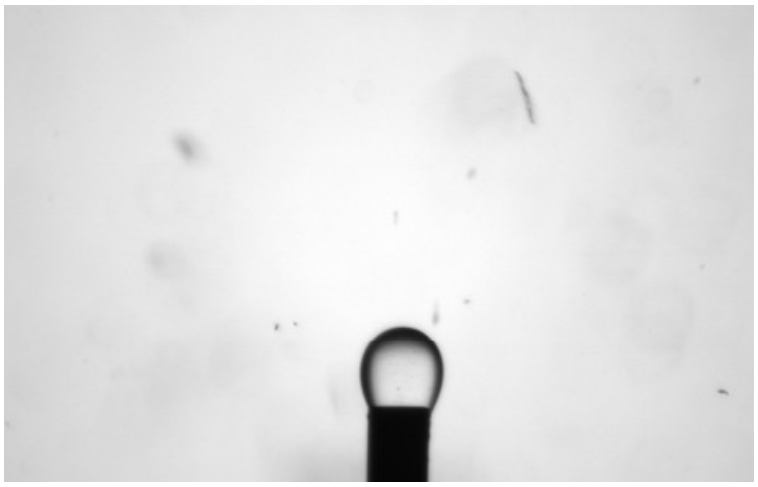

Figure 21: A Droplet of Alginate Before Releasing into an Oil Medium from a Hooked 30-Gauge Needle.

Stagnant droplets of alginate in oil resulted in an average surface tension coefficient of 0.622mN/m over 5 tests. We also tried one test with the stagnant drop, but FSH-oil was increased to 3% volume in the oil medium, this test resulted in a lower surface tension coefficient of 0.43mN/m. A dynamic droplet test was conducted to try and heighten the accuracy of the experiment for a surface tension coefficient that better represented what we would see in droplet generation. The resulting plot of dynamic droplets being released into the oil is shown in figure 22 below.

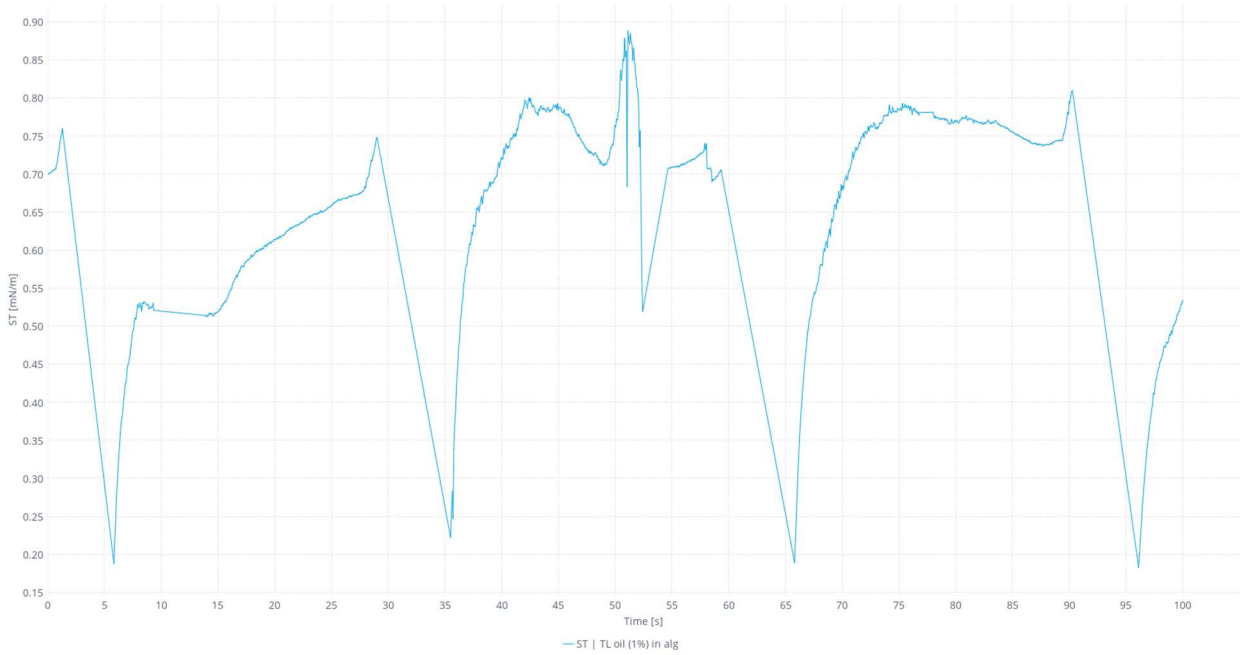

Figure 22: Dynamic Surface Tension Coefficient Between Alginate and Oil over Time

From these results we can characterize each peak to a droplet being formed. Averaging the peaks we obtain a surface tension coefficient of 0.8mN/m. Using this new value in ANSYS results in figure 23 below.

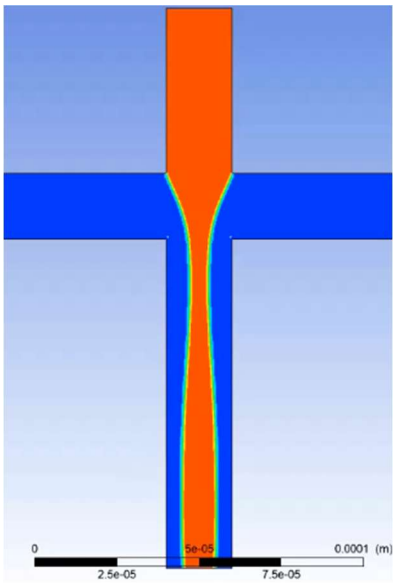

Figure 23: 20-Micron Junction Simulation with Q=3/1 and STC=0.1mN/m

The capillary number from this simulation setup was equal to 0.091, a very large value we had not seen in the other simulations with the surface tension coefficient set to 21.75mN/m.

Physical Experiment on High-Efficiency Droplet Production

We assessed our novel multi-channels system for droplet production as various flow rate ratio (Q) as listed in table 2. Images of droplets were taken and analyzed after each experiment.

Table 2: Trials with Their Corresponding Flow Rate Values Selected

Device Used	Oil Flow Rate (μL/min)	Alginate Flow Rate (μL/min)	Flow Rate Ratio (Q)
20μm Single Outlet	3	1	3
20μm Triple Outlet	9	1	9
20μm Triple Outlet	9	3	3
30μm Triple Outlet	9	2	4.5
30μm Triple Outlet	13.5	4.5	3
50μm Triple Outlet	9	3	3
50μm Triple Outlet	22.5	7.5	3

All experiments from table 2 utilized a 2% FSH solution in FO-101, all other parameters were identical as mentioned in the materials and methods for physical testing setup. Figures 24-30 below show raw images at 10x and 20x zoom of each trial.

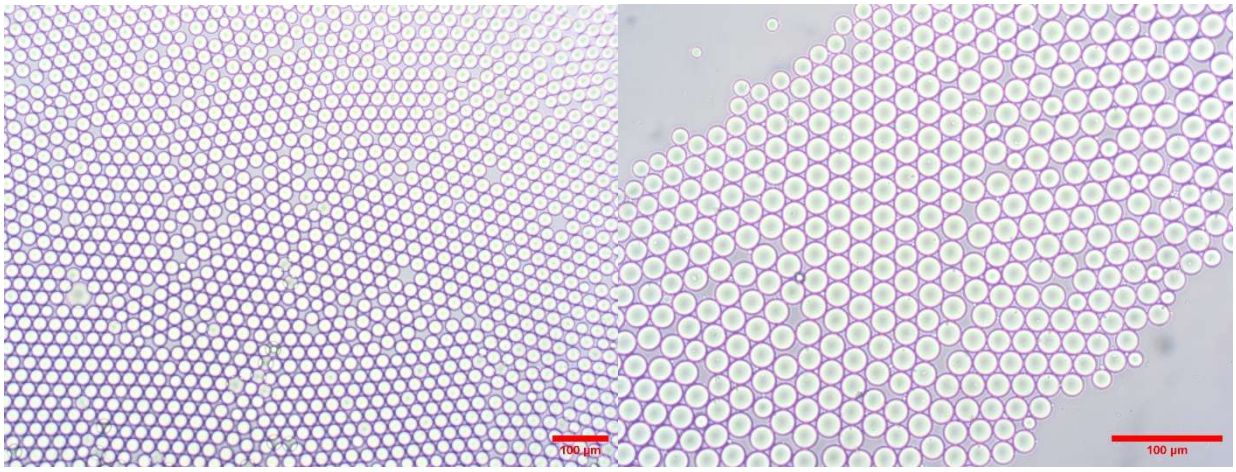

Figure 24: Droplet Images from 20µm Single Outlet Q=3/1 at 10x (left) and 20x (right)

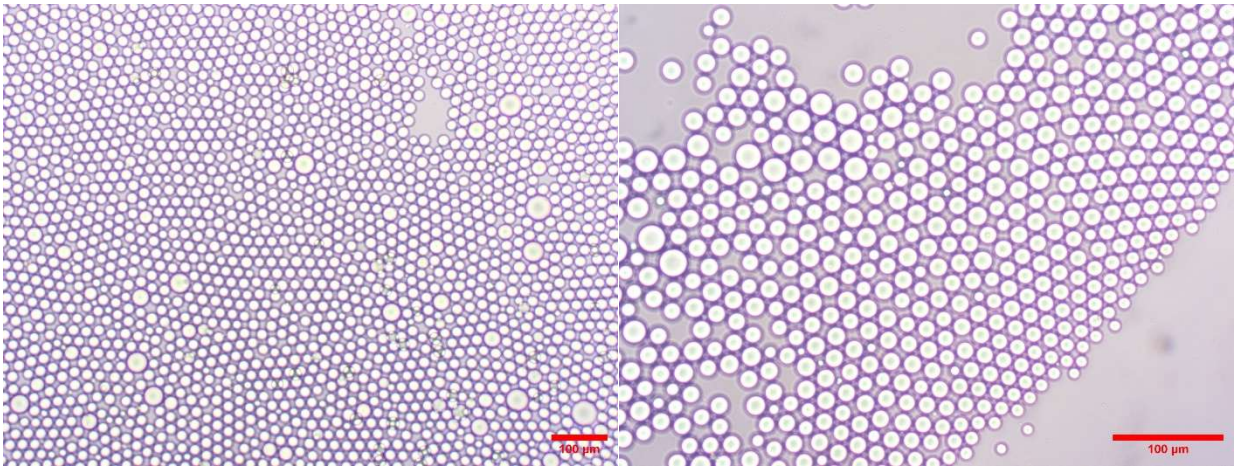

Figure 25: Droplet Images from 20µm Triple Outlet Q=9/1 at 10x (left) and 20x (right)

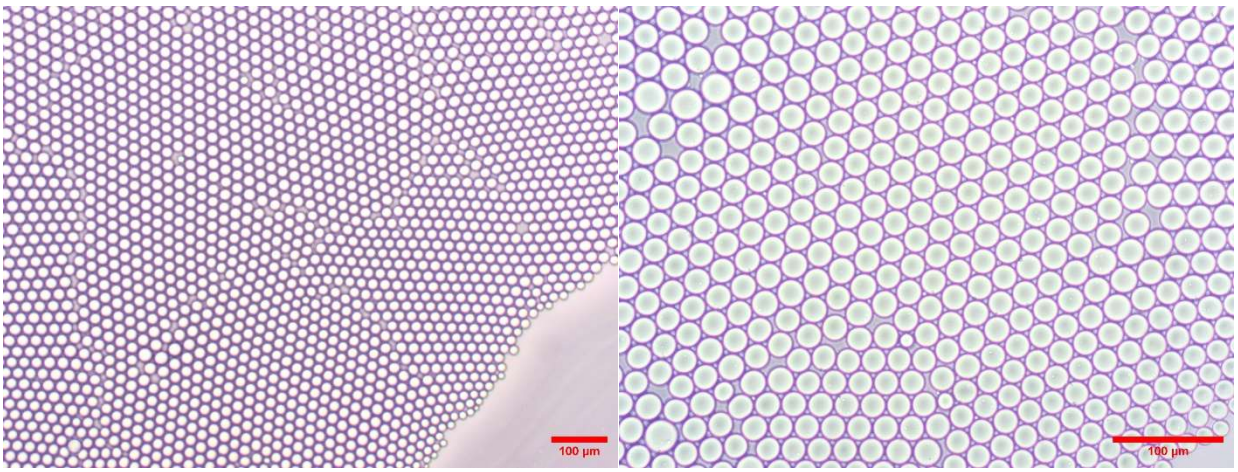

Figure 26: Droplet Images from 20µm Triple Outlet Q=9/3 at 10x (left) and 20x (right)

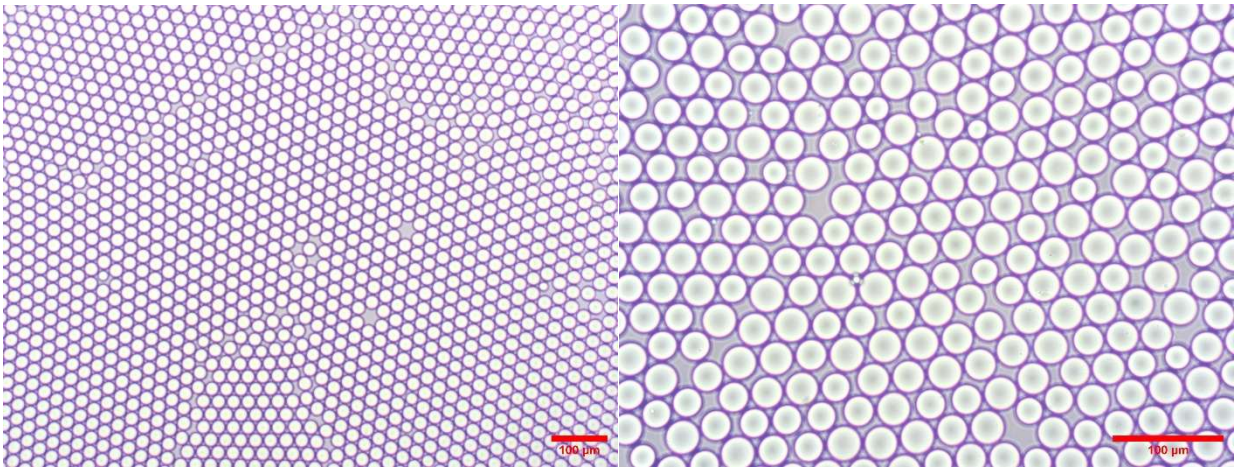

Figure 27: Droplet Images from 30µm Triple Outlet Q=9/2 at 10x (left) and 20x (right)

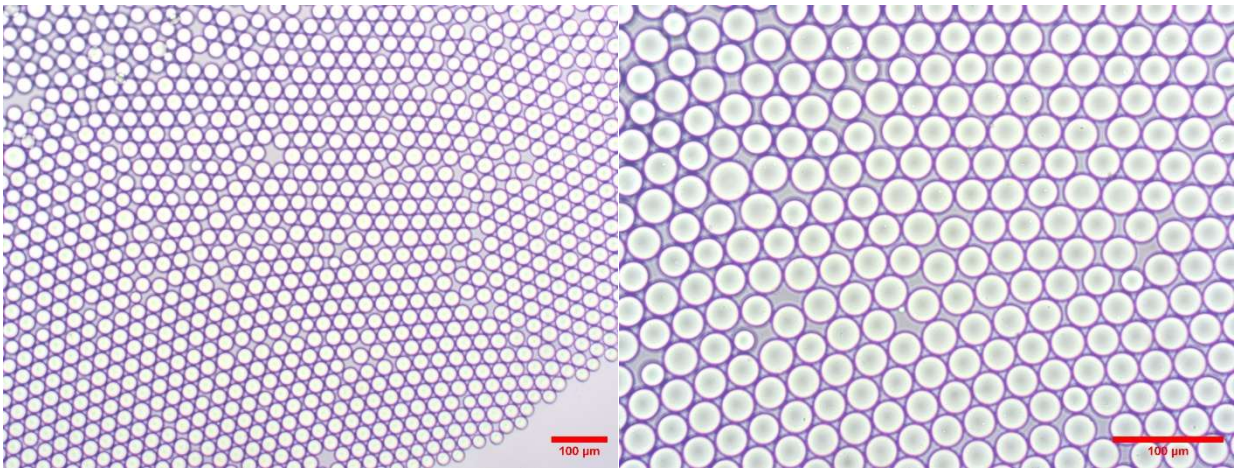

Figure 28: Droplet Images from 30µm Triple Outlet Q=13.5/4.5 at 10x (left) and 20x (right)

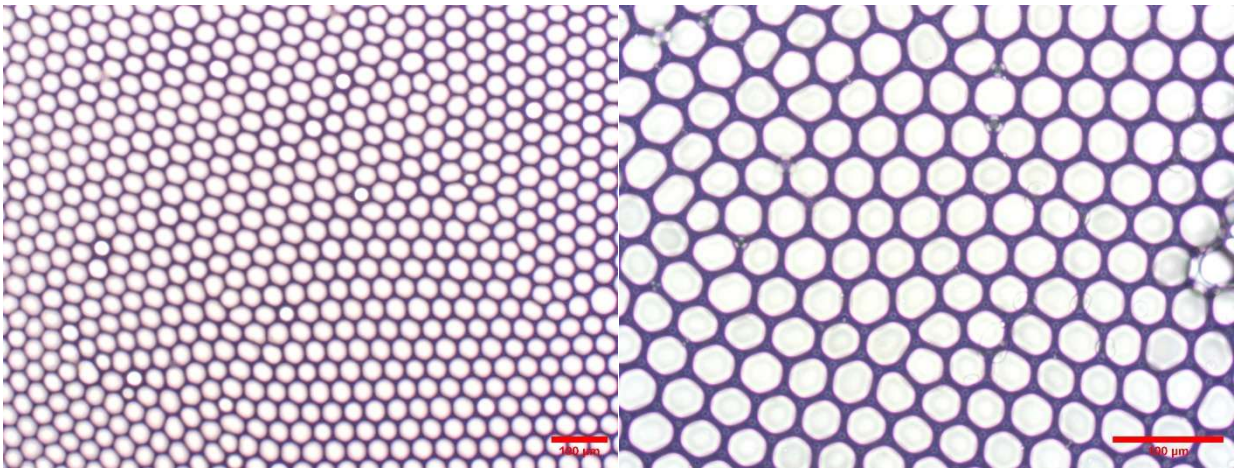

Figure 29: Droplet Images from 50µm Triple Outlet Q=9/3 at 10x (left) and 20x (right)

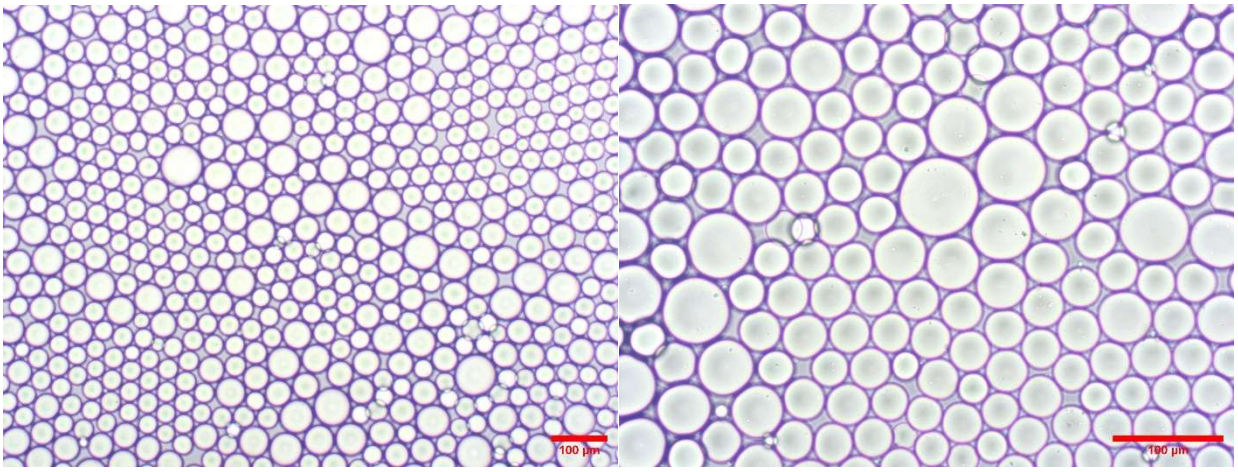

Figure 30: Droplet Images from 50µm Triple Outlet Q=22.5/7.5 at 10x (left) and 20x (right)

From these images, 30 randomly selected droplets were measured from each of the 20x zoom images. Droplets were measured with a calibrated Swift Imaging software, the same used to take the images. The droplet diameter analysis, homogeneity of droplet formation and droplet formation frequency are summarized in figures 31, 32, 33 and table 3.

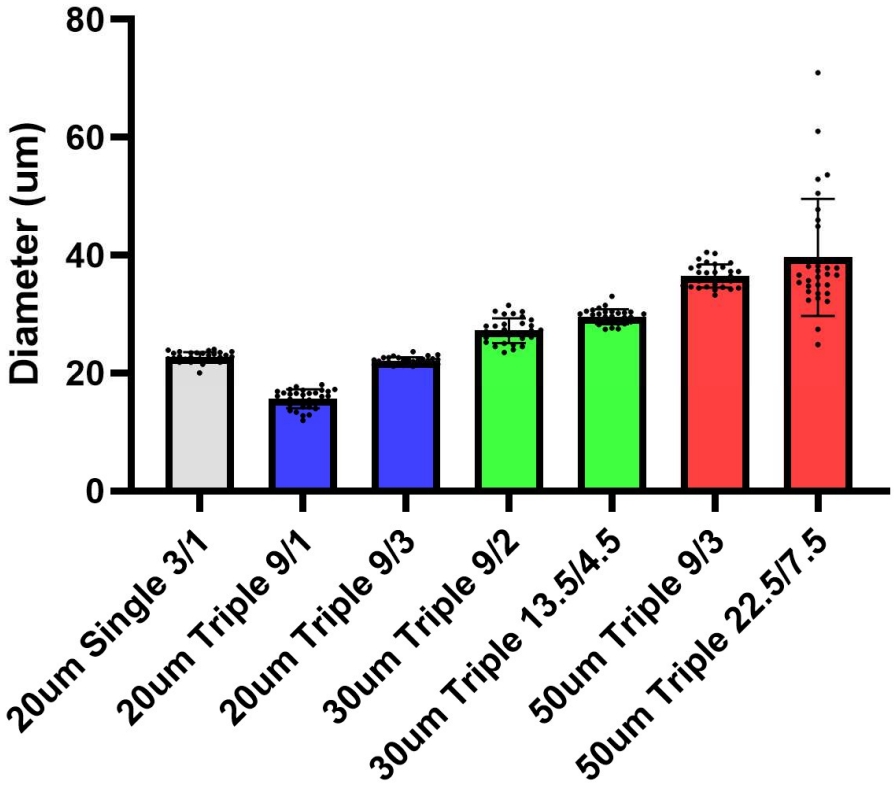

Figure 31: Column Plot Showing n=30 Droplet Diameter Measurements from each Experiment

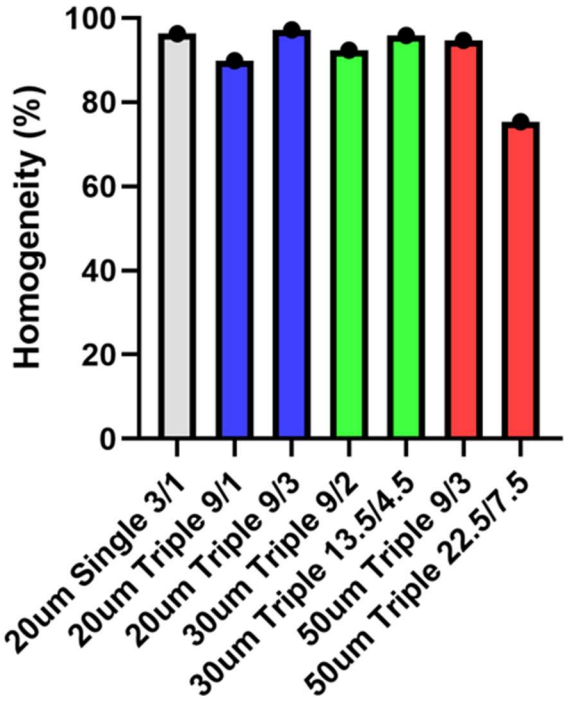

Figure 32: Homogeneity of Droplets as a Function of Flow Rates and Junction Dimension

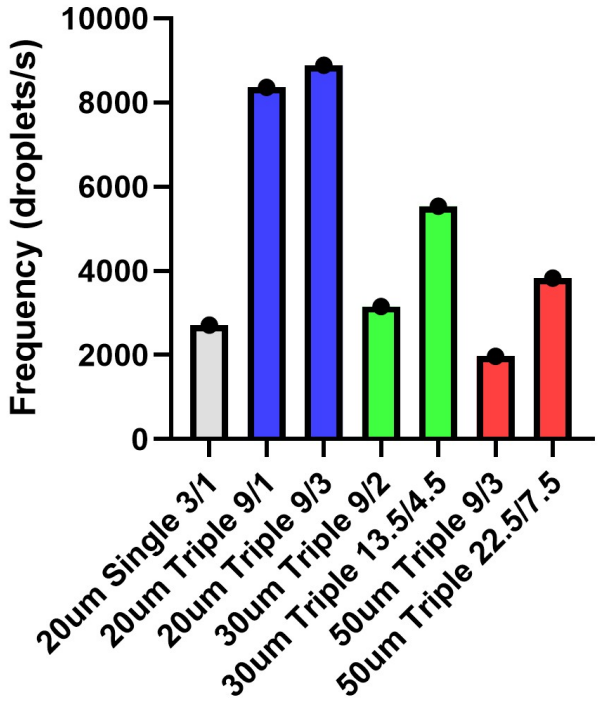

Figure 33: Droplet Formation Frequency as a Function of Flow Rates and Junction Dimension

Table 3 below contains the calculated mean volume for each test as well as the values for the homogeneity and frequency of droplets per second.

Table 3: Mean Volume, COV and Frequency in Droplets per Second

Trial Name	Mean Droplet Volume (μm^3)	Homogeneity (%)	Frequency (droplets/second)
20µm Single Q=3/1	6,148	96.28%	2711
20µm Triple Q=9/1	1,992	89.9%	8366
20µm Triple Q=9/3	5,625	97.22%	8889
30µm Triple Q=9/2	10,563	92.4%	3156

30µm Triple Q=13.5/4.5	13,536	95.89%	5541
50µm Triple Q=9/3	32,035	94.65%	1561
50µm Triple Q=22.5/7.5	32,626	75.41%	3831

In figure 31 we see droplets comparable in size between the 20µm devices, when the flow rate ratio is held constant at Q=3 between the two types of devices droplet size is remarkably similar. Increasing Q=9 as seen in the second column, decreases droplet size. An increase in droplet size as the junction geometry increases is also noticeable. In figure 32 we see that the coefficient of variation is at its lowest when Q=3 besides the last test on the 50µm triple outlet device. In figure 33 we also see that frequency is at its highest for the 20µm triple outlet device, increasing junction width and therefore cross-sectional area decreases droplet frequency. For table 3, mean volume was calculated to compare with our ANSYS results as well as to find the frequency as seen in equation 5.

DISCUSSION

ANSYS Simulations

From our results in table 1 we see how increasing oil flow rate while leaving the alginate flow rate constant will increase droplet frequency. This trend is expected as the oil is now moving much faster through the junction which would result in an increased production rate of droplets while sacrificing droplet length. While the alginate is still subject to the same flow rate of 1μL/min, the increased shear force of the oil phase causes droplets to detach earlier, resulting in smaller droplets at a higher generation frequency. The capillary number here is also greater than 0.01 which is referenced as the limit for producing droplets in the dripping regime. Pushing past this value may result in a jetting regime which is notorious for heterogeneous droplet production. Through these simulations we did not see droplets produced within the jetting regime but rather in a dripping regime, hinting that within a smaller geometry the capillary number range for the dripping regime may reside within another limit. It is also worth noting that the surface tension coefficient used for these ANSYS simulations was half of that found between FO-101 and water: 21.75mN/m, after tensiometer testing this value was altered to better represent physical testing which will be discussed further. What we can expect to see in physical testing is droplet size is subject to change due to any change in flow rate even if the ratio is the same value. Increasing or decreasing flow rate will in turn change the energy being put into the system, at such a small scale of device we can expect any change in energy will influence droplet size. This proportional oil flow increase also doubles the capillary number, showing a linear trend between the two. Frequency of droplets has also been increased by nearly double. The overall trend from the 20μm junction shows that frequency of droplets can be increased while maintaining homogeneity within the system by taking into the account the capillary number to

ensure viscous flow is not overpowering interfacial tension between the two fluids. We can expect a range of droplet sizes from the 20µm junction device, but these ranges are confined by the cross-sectional area of the device. With this idea, we can create larger droplets by increasing the cross-sectional area of the device by increasing junction width to 30µm and 50µm. This is another expected trend, as cross-sectional area increases, velocity will decrease to maintain the same flow rate as they are directly proportional as seen in equation 6 below.

$$Q\left(\frac{L}{s}\right) = v\left(\frac{m}{s}\right) * A(m^2) \qquad (6)$$

Velocity of the fluids has therefore decreased with an increase in cross-sectional area and constant flow rate, meaning the viscous and shear force of the oil phase has been decreased, leading to a lower frequency and capillary number. With this subsequential decrease in oil speed, alginate can fill a larger portion of the junction before succumbing to the oil's shear force and being pinched off to generate a droplet, leading to larger droplets. Again, we are seeing how changing cross-sectional area has large effects on droplet production. Increasing cross-sectional area has decreased fluid speed which in turn decreases shear and viscous forces while the surface tension coefficient remains constant, droplet size and behavior therefore is altered due to this jump in junction width. To try and retain droplet size amongst different geometries, the working hypothesis would be to try and match fluid speed as well as the flow rate ratio. Doing so will in theory match the viscous and shear forces amongst the different geometries. Utilizing equation 6 we can calculate the flow rates needed for each geometry to have corresponding fluid speeds in all devices. Ensuring a constant fluid amongst different geometries will help us better understand how the geometry itself will affect droplet size and frequency.

Tensiometer Testing

Original tensiometer testing consisted of utilizing a stagnant droplet of alginate suspended in the surrounding oil medium which had 1% volume of FSH-oil. From these results we see that increasing FSH-oil does in fact decrease surface tension coefficient which will in turn increase capillary number. Increasing surface tension coefficient helps with creating smaller droplets as well as keeping formed droplets from combining into each other. One oversite from these tests is that droplet formation is highly dynamic which may influence the surface tension coefficient. To test this hypothesis, we conducted a test where we allowed droplets to form and increased the testing time to capture surface tension coefficient as droplets were generated from the hooked 30-gauge needle. These results were shown in figure 22 where each peak of the graph corresponds to a droplet being generated. Each peak was averaged for a value of 0.8mN/m, which was larger than the stagnant drop test result of 0.622mN/m. Utilizing this new value, we revisited our ANSYS simulations. When updating the simulation to contain a rounded-up surface tension coefficient value of 1mN/m we see the following results as shown in figure 23. As we can see, the resulting simulation contains one long jet of the alginate phase. The capillary number was increased because it is inversely proportional to surface tension coefficient. What this large value signifies is that the viscous forces at the droplet interface are too extreme, it overpowers the interfacial tension of the system and fails to generate droplets. This resulting simulation proved troublesome as we were now unsure if these parameters would result in droplets during physical testing. We proceeded with physical testing to prove or disprove our ANSYS results.

Physical Droplet Production

Contrary to what our latest simulation showed, droplets were able to be produced efficiently and effectively. All successful physical droplet tests also utilized an increase in FSH-

oil percentage at 2% of the oil phase. For our physical experiments we could qualify 3 states of droplet production. One being purely oil as it was moving at a faster rate and would reach the collection tube first, another being unstable droplet production where large, clear droplets would be moving through the outlet tubes and the last being stable droplet production which could be visually described as white emulsions moving through the outlet tubes. The unstable droplet state resulted from either a squeezing or jetting regime which produces large, heterogeneous droplets as seen below in figure 34.

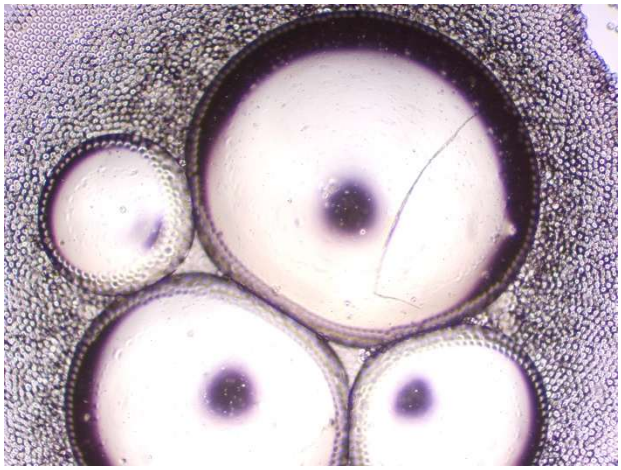

Figure 34: Droplets Resulting from Unstable Droplet Production

The exact regime whether it be squeezing from too low of a capillary number or jetting from too high of a capillary number could not be visualized as we did not have the capabilities to view the junction during droplet production. After seeing how low of a surface tension coefficient we are dealing with, we can infer that the unstable droplets resulted from a jetting regime. Increasing FSH-oil to 2% also resulted in less tests where unstable droplets were being produced. Another factor which could have contributed to unstable droplets would be debris stuck in the channels, possible early cross-linking between the oil and alginate in the junction and the mechanism for droplet collection from the outlets. Debris which was present in the microchannels could be

combated with the oil phase rushing through the micro-channels first to flush out any small debris. Early cross-linking was not an issue as the presence of calcium carbonate and acetic acid were low at concentration for our tests. In figure 13 we see three tubes protruding from their respective outlets, this form of collection was used for the 20µm triple 9/1 test, the 30µm triple 9/2 test and the 50µm triple 9/3 test. After having instances of unstable droplet formation, a new method utilizing cut, gel-loading pipette tips that were open from both ends was used for the remaining tests as seen in figure 35 below.

Figure 35: Droplet Collection Process Utilizing Cut, Gel-Loading Pipette Tips

With this new method we had more stable which led us to revisit and conduct the 20µm triple 9/3 test, 30µm triple 13.5/4.5 test and the 22.5/7.5 test, all of which failed with the previous outlet collection setup. What we can see from figure 28 is how droplet diameter is dependent on flow rate ratio and junction geometry. Starting with the 20µm triple Q=9/1 test, we see our droplets are at the lowest diameter which matches our results from earlier ANSYS simulations since this test utilized the largest Q value of 9. Increasing this ratio is what causes smaller droplets to form. For our first 30µm triple outlet device we chose Q=9/2 because when implementing Q=9/2 on our 20µm triple outlet device, we saw multiple instances of instable

droplet production. Inferring that this was the upper limit for the 20µm triple outlet device utilizing the previous droplet collection method, we utilized Q=9/2 on our 30µm triple outlet device. This test resulted in droplets larger in diameter than the previous, further reinforcing how an increase to cross-sectional area in junction geometry will result in larger droplets. We also see the alginate flow rate can surpass the former limit seen in the 20µm triple outlet device when utilizing the previous collection method. When the flow rate ratio was increased to Q=9/3 on the 30µm triple outlet device, we saw instability in droplet formation which led us to utilize this test on the largest junction, the 50µm triple outlet device. The 50µm device test resulted in stable droplets that had a much larger jump in diameter due to the cross-sectional area increase. What we can infer from these tests is that larger junctions can withstand higher energy inputs, yet we lose the ability to create smaller droplets. The final four tests have all utilized the new droplet collection method utilizing gel-loading pipette tips to reduce pressure from the outlet back onto the system. The 20µm single outlet device at Q=3/1 (figure 31 gray column) had a resulting average diameter per droplet like that of the 20µm triple outlet device at Q=9/3 (figure 31 second blue column). What this shows is that we can closely replicate our results from the original device by tripling the flow rates for our novel, parallel flow devices. For the 30µm triple outlet device and the 50µm triple outlet device we evaluated Q=13.5/4.5 and Q=22.5/7.5 respectively to match the relative fluid velocity used on the 20µm junction devices. What we see is an increase in droplet diameter in both cases (figure 31 green and red columns), however the diameters do not increase by much when in comparison with their respective counterparts in the same figure. This observation could reinforce that droplet size for each geometry is within its own set of minimum and maximum values and droplets outside of these limits result in instable generation rather than smaller and larger diameters. In theory, for a larger cross-sectional area,

keeping the velocity the same by increasing flow and keeping Q at the same ratio should result in similarly sized droplets across all devices. This was however disproven through our experiments. We believe this to be due to the influence geometry has on the resulting droplets, increasing the cross-sectional area has resulted in droplets larger than previously sized device, even with our attempts to balance forces. Droplet size is heavily reliant on the geometry used. In figure 29 we see the coefficient of variance (COV) from our randomly selected 30 droplets. Here, a lower value corresponds to higher homogeneity amongst the droplets. Our aim was to achieve 90% or higher homogeneity in the resulting droplets. Why 100% was not achieved was due to imperfections in our system such as small debris or moments of instable flow due to imbalances of flow within the device. All devices except for the 50µm triple outlet with Q=22.5/7.5 reached this 90% threshold. Shown in figure 27, we see droplets of varying sizes in our 10x and 20x zoomed images. This heterogeneity in droplet size was most likely due to the energy input within the device. These two flow rates for oil and alginate were not utilized before and we believe we are seeing an upper threshold for the device. We did not view any instability in droplet formation as the device was running but we can say for certain it was prevalent due to the COV calculated and resulting images. Figure 30 shows frequency in droplets per second for each experiment. What is important to note is the difference between the 20µm single outlet device with Q=3/1 and the 20µm triple outlet device with Q=9/3 which are replicates of the same parameters on two different devices. The frequency has increased in our device by 3.3 times. This is not strictly a 3 times increase is because the droplets produced from the triple outlet device were slightly smaller than the single outlet device. We also see the same trend in all three triple outlet devices, increasing individual flow rate values does in fact increase frequency of droplets. Increasing cross-sectional area does also decrease frequency due to velocity of fluid decreasing.

Comparing ANSYS and Physical Testing

Contrary to what ANSYS results led us to believe, physical testing produced homogeneous droplets and did not result in one long jet of the alginate phase. We believe this to be contributed to ANSYS parameters not being fully accurate to our physical tests or that the surface tension coefficient is not truly equal to 0.8mN/m when subject to such a small and highly dynamic environment. Our capabilities with the tensiometer did not allow us to create droplets at a scale as small or as fast as the ones seen in our physical results but we do know the tensiometer utilizes droplet size and shape to find the surface tension coefficient between two fluids. The setup of droplet production for the tensiometer did not accurately represent the system utilized by the device which could have altered the resulting values. Comparing results between the physical and simulated Q=3/1 20µm junction devices, we see the physical test gave a droplet volume of 6,148um^3 and the simulated test gave a droplet volume of 5,542um^3. We already know the surface tension coefficient between these two experiments are not the same, but this still is a notable difference showing there is need to refine ANSYS parameters to verify our model to the physical results.

CONCLUSION

Synthesizing microgels via a flow-focusing microfluidic droplet device depends on immiscible fluids, flow rates, geometry of the junction as well as device design. For our approach to generate microgels we utilized a fluorinated oil as the continuous phase, and an alginate based aqueous solution for the dispersed phase. These two fluids are immiscible and with the addition of surfactant to the oil phase we can synthesize droplets that do not coagulate into larger droplets. The continuous phase contains acetic acid, and the dispersed phase contains calcium carbonate providing alginate with the calcium ions needed to crosslink once a droplet is formed. Taking inspiration from a working, previously designed flow-focusing device, we were able to create a device that consists of three junctions running in parallel with one inlet for each phase. This novel device allowed us to continue using a dual driving syringe pump while increasing yield of homogeneous droplets. By testing different flow rates and junction sizes in both ANSYS and physical experiments, we were able to quantify and predict droplet size, frequency, and homogeneity. Droplet size is dependent on both shear force of the fluids moving through the microchannels as well as the surface tension coefficient between both fluids. Shear force is dependent on fluid speed which correlates to the flow rate and dimensions of the microchannel. Increasing shear force by manipulating these variables will result in a faster generation of droplets. We must however consider the surface tension coefficient between two fluids as the ratio between the viscous forces such as shear force and the interfacial tension needs to be within a specific range to ensure droplets are generated within a stable regime. Extensive testing of these parameters resulted in a novel device which produced 3.3 times higher droplet production, while maintaining droplet homogeneity for over 97%, therefore significantly increasing the yield of homogenous droplet formation when compared to the existing device.

REFERENECES

1. Whitesides, G. M. The origins and the future of microfluidics. *Nature* **442**, 368–373 (2006).
2. Bruijns, B., van Asten, A., Tiggelaar, R. & Gardeniers, H. Microfluidic Devices for Forensic DNA Analysis: A Review. *Biosensors* **6**, 41 (2016).
3. Takken, M. & Wille, R. Accelerated Computational Fluid Dynamics Simulations of Microfluidic Devices by Exploiting Higher Levels of Abstraction. *Micromachines* **15**, 0 (2024).
4. Lambert, C. L. G., van Mierlo, G., Bues, J. J., Guillaume-Gentil, O. J. & Deplancke, B. The evolution of DNA sequencing with microfluidics. *Nat. Rev. Genet.* **26**, 1–2 (2025).
5. Zhai, J. *et al.* Drug screening on digital microfluidics for cancer precision medicine. *Nat. Commun.* **15**, 4363 (2024).
6. Sun, J., Warden, A. R. & Ding, X. Recent advances in microfluidics for drug screening. *Biomicrofluidics* **13**, 061503 (2019).
7. Sackmann, E. K., Fulton, A. L. & Beebe, D. J. The present and future role of microfluidics in biomedical research. *Nature* **507**, 181–189 (2014).
8. Xiang, N. & Ni, Z. Microfluidics for Biomedical Applications. *Biosensors* **13**, 161 (2023).
9. Deliorman, M., Ali, D. S. & Qasaimeh, M. A. Next-Generation Microfluidics for Biomedical Research and Healthcare Applications. *Biomed. Eng. Comput. Biol.* **14**, 11795972231214387 (2023).
10. Droplet microfluidics for biomedical applications: emerging trends and future developments | Microsystems & Nanoengineering. https://www.nature.com/articles/s41378-026-01175-7.

11. Ghobadi, F., Saadatmand, M., Simorgh, S. & Brouki Milan, P. Microfluidic 3D cell culture: potential application of collagen hydrogels with an optimal dose of bioactive glasses. *Sci. Rep.* **15**, 569 (2025).
12. Jiang, Z., Xia, B., McBride, R. & Oakey, J. A microfluidic-based cell encapsulation platform to achieve high long-term cell viability in photopolymerized PEGNB hydrogel microspheres. *J. Mater. Chem. B* **5**, 173–180 (2017).
13. Hidalgo San Jose, L., Stephens, P., Song, B. & Barrow, D. Microfluidic Encapsulation Supports Stem Cell Viability, Proliferation, and Neuronal Differentiation. *Tissue Eng. Part C Methods* **24**, 158–170 (2018).
14. Li, F., Truong, V. X., Thissen, H., Frith, J. E. & Forsythe, J. S. Microfluidic Encapsulation of Human Mesenchymal Stem Cells for Articular Cartilage Tissue Regeneration. *ACS Appl. Mater. Interfaces* **9**, 8589–8601 (2017).
15. Duncan, J. L., Arroyo, J. P. & Davalos, R. V. Microfluidics for cell therapy and manufacturing in oncology and regenerative medicine. *Lab. Chip* **26**, 1566–1587 (2026).
16. Samadi, A. *et al.* Cell Encapsulation and 3D Bioprinting for Therapeutic Cell Transplantation. *ACS Biomater. Sci. Eng.* **9**, 1862–1890 (2023).
17. Kim, H. *et al.* 3D Bioprinting of Cellular Therapeutic Systems in Ophthalmology: from Bioengineered Tissue to Personalized Drug Delivery. *Curr. Ophthalmol. Rep.* **13**, 10 (2025).
18. Three-Dimensional Printing/Bioprinting and Cellular Therapies for Regenerative Medicine: Current Advances. https://www.mdpi.com/2079-4983/16/1/28.
19. Wang, Z. & Kelley, S. O. Microfluidic technologies for enhancing the potency, predictability and affordability of adoptive cell therapies. *Nat. Biomed. Eng.* **9**, 803–821 (2025).

20. Controlled Deposition of 3D Matrices to Direct Single Cell Functions - Wong - 2020 - Advanced Science - Wiley Online Library. https://advanced.onlinelibrary.wiley.com/doi/full/10.1002/advs.202001066.
21. Wong, S. W. *et al.* Inhibition of aberrant tissue remodelling by mesenchymal stromal cells singly coated with soft gels presenting defined chemomechanical cues. *Nat. Biomed. Eng.* **6**, 54–66 (2022).
22. Liu, D., Xuanyuan, T., Liu, X., Fu, W. & Liu, W. Massive and efficient encapsulation of single cells in monodisperse droplets and collagen-alginate microgels using a microfluidic device. *Front. Bioeng. Biotechnol.* **11**, 1281375 (2023).
23. Tang, T., Zhao, H., Shen, S., Yang, L. & Lim, C. T. Enhancing single-cell encapsulation in droplet microfluidics with fine-tunable on-chip sample enrichment. *Microsyst. Nanoeng.* **10**, 3 (2024).
24. Nakamura, M. *et al.* Microfluidic device for the high-throughput and selective encapsulation of single target cells. *Lab. Chip* **24**, 2958–2967 (2024).
25. Ling, S. D., Geng, Y., Chen, A., Du, Y. & Xu, J. Enhanced single-cell encapsulation in microfluidic devices: From droplet generation to single-cell analysis. *Biomicrofluidics* **14**, 061508 (2020).
26. Mapping flow-focusing microfluidic droplet formation to determine high-throughput droplet generation configurations - ScienceDirect. https://www.sciencedirect.com/science/article/pii/S2590123023002529.
27. Immiscible Liquid - an overview | ScienceDirect Topics. https://www.sciencedirect.com/topics/engineering/immiscible-liquid.

28. Venkateshwarlu, A. & Bharti, R. P. Effects of capillary number and flow rates on the hydrodynamics of droplet generation in two-phase cross-flow microfluidic systems. *J. Taiwan Inst. Chem. Eng.* **129**, 64–79 (2021).
29. Mulligan, M. K. & Rothstein, J. P. Scale-up and control of droplet production in coupled microfluidic flow-focusing geometries. *Microfluid. Nanofluidics* **13**, 65–73 (2012).
30. Navier-Stokes Equations in Ansys Fluent | Education Resources. https://www.ansys.com/academic/educators/education-resources/exact-solutions-of-navier-stokes-equations-using-ansys-fluent-software.
31. FO101.
32. Pendant drop method for surface tension measurements. https://www.biolinscientific.com/blog/pendant-drop-method-for-surface-tension-measurements.
33. Tomić, S. Lj. *et al.* Alginate-Based Hydrogels and Scaffolds for Biomedical Applications. *Mar. Drugs* **21**, 177 (2023).
34. Fluent Theory Guide. https://ansyshelp.ansys.com/public/account/secured?returnurl=/Views/Secured/corp/v242/en/flu_th/flu_th.html.

APPENDIX

A: ANSYS Fluent Setup Parameters

For the ANSYS setup parameters, the scheme was listed as PISO for the algorithm which controls the manner in which pressure and velocity are updated when the pressure-based solver is used, PISO worked best in our case since are simulation was transient and our time step was very small[34]. The gradient was Green-Gauss Cell Based which is needed for constructing values of a scalar at the cell faces while also computing secondary diffusion terms and velocity derivatives[34]. Green-Gauss computes the gradient of the scalar at the cell center with the summation being over all the faces enclosing the cell[34]. The pressure interpolation scheme was set to PRESTO! which stands for pressure staggering option and is the standard for multiphase simulations, this scheme uses the discrete continuity balance for a "staggered" control volume about the face to compute the "staggered" pressure[34].